Master's thesis

NTNU
Norwegian University of Science and Technology
Faculty of Natural Sciences
Department of Physics

Stene, Sigurd

The Effects of Wide-angle Scattering on Coherent Diffraction Imaging

A numerical study

Master's thesis in Nanotechnology
Supervisor: Chattopadhyay, Basab
Co-supervisor: Breiby, Dag Werner
July 2023

Meg

NTNU
Norwegian University of
Science and Technology

Stene, Sigurd

The Effects of Wide-angle Scattering on Coherent Diffraction Imaging

A numerical study

Master's thesis in Nanotechnology
Supervisor: Chattopadhyay, Basab
Co-supervisor: Breiby, Dag Werner
July 2023

Norwegian University of Science and Technology
Faculty of Natural Sciences
Department of Physics

NTNU
Norwegian University of
Science and Technology

ABSTRACT

The effects of wide-angle scattering on Coherent X-ray Diffraction Imaging (CDI) have been explored numerically to investigate whether the intensity lost due to Bragg scattering might have a negative impact on the phase retrieval process.

CDI is a nondestructive, three-dimensional imaging technique utilising phase retrieval algorithms to digitally reconstruct an object from a set of its small-angle diffraction patterns measured in the Fraunhofer limit. The technique is routinely able to resolve features down to tens of nanometers, and with the development of in situ CDI, several new applications can be envisaged.

However, today's phase retrieval algorithms assume that all the incoming radiation will contribute to the small-angle diffraction pattern for all the orientations of the sample. This assumption is well-founded for non-crystalline samples, for which the technique initially was developed. However, for crystalline samples, there will be a measurable signal at the wide-angle detector, meaning that some of the incoming intensity has been scattered off the sample. If a sufficiently large portion of the incoming beam is scattered, the author has previously shown that these losses might have serious negative impacts on the reconstruction quality, up to a point where the applied phase retrieval algorithm could not reconstruct the examined object [49].

It was however necessary to assume a large amount of scattered intensity, i.e. approximately 50% of the incoming beam, to see the negative effects. Therefore, it remained to investigate whether the negative effects could be seen if the intensity losses matched those in a real CDI experiment. To decide how much of the incoming intensity is lost due to the wide-angle scattering, rocking curves of simulated aragonite crystallites, with diameters ranging from approximately 75 nm to 500 nm, have been calculated using the kinematical approximation. No absolute intensity reduction could be decided, but the range of sample orientations which gave a wide-angle signal was found, and this range was significantly narrower than what had been assumed in the previous work [49].

Building on the new range of $\pm 0.1^\circ$, the effects of Bragg scattering on CDI were examined anew. By calculating the diffraction pattern of a known object and reducing the intensity for some projections, the effects of the phase retrieval process were studied. A reduction in the reconstruction quality was observed given that the intensity reduction was large enough. However, the phase retrieval algorithm was able to reconstruct the sample for all the intensity reductions, and only minor deviations were observed. It is therefore unlikely that Bragg scattering will have a significant negative effect on the phase retrieval process.

However, before drawing any final conclusions, further analysis of the absolute intensity reductions must be performed. If the reductions appear to be of the order which gave a reduced reconstruction quality in this thesis, i.e. 30% or more, it would be advisable to design an experiment which could accurately measure the relation between the incoming beam and the beam scattered to the wide-angle detector.

SAMMENDRAG

De potensielle negative effektene av vidvinkel-spredning på fasegjenvinningsprosessen i koherent røntgendiffraksjonsavbildning (CDI) har blitt undersøkt ved bruk av numeriske beregninger.

CDI er en avbildningsmetode som kan lage en digital, tredimensjonal kopi av en prøve fra et sett med småvinkel Fraunhofer-diffraksjonsmønster. Metoden er særlig ettertraktet da den kan finne de tredimensjonale detaljene av prøven, med en oppløsning på rundt et titalls nanometer, uten å kutte den opp. Teknikken har allerede vist at den kan bidra med nyttig informasjon på tvers av mange fagfelt, og med tidsoppløst CDI på trappene kan man se for seg en rekke nye bruksområder.

Det finnes derimot et problem med dagens fasegjenvinningsalgoritmer, og det er at de antar at all den innkommende intensiteten vil bidra til småvinkel diffraksjonsmønstrene for hver orientering av prøven. Denne antagelsen vil sannsynligvis være riktig for ikke-krystallinske prøver, som teknikken først ble utviklet for å avbilde, men for krystallinske prøver måler man derimot et sterkt signal ved vidvinkel-detektoren. Spørsmålet blir derfor hva forholdet mellom denne spredte intensiteten og den innkommende intensiteten er, og hvordan forholdet påvirker resultatene i et CDI-eksperiment. Tidligere har undertegnede ved bruk av numeriske simuleringer vist at vidvinkel-spredning kan ha en betydelig innvirkning på rekonstruksjonskvaliteten, opp til et punkt hvor fasegjenvinningsalgoritmene ikke klarte å gjenskape prøven [49].

I disse beregningene ble det derimot antatt en forholdsvis stor intensitetsreduksjon. Det var derfor nødvendig å undersøke om de negative effektene fortsatt ville være til stede hvis en mer realistisk fordeling av vidvinkel-spredningen ble brukt i simuleringene. For å bestemme denne fordelingen ble såkalte *rocking curves* av ulike simulerte aragonitt krystallitter beregnet. Dessverre ble det ikke funnet en løsning for å normalisere den spredte intensiteten med hensyn på den innkommende strålen. Det ble derimot funnet et nytt anslag på hvor stort vinkelspenn av prøveorienteringer som vil gi en målbar mengde spredning.

Ved å bruke det nye spennet på $\pm 0.1^\circ$, som var betydelig smalere enn spennet som ble antatt i det tidligere arbeidet [49], samt de samme intensitetsreduksjonene som i [49], avtok de negative effektene betraktelig. Små forverringer i rekonstruksjonskvaliteten ble observert for de største intensitetsreduksjonene, men alle rekonstruksjonene var kvalitativt lik den originale prøven, og det var kun mindre lokale variasjoner som skilte de ulike rekonstruksjonene. Det anses derfor som usannsynlig at vidvinkel-spredning har en betydelig påvirkning på fasegjenvinningsprosessen.

Selv om effektene av vidvinkel-spredning sannsynligvis er små, om merkbare i det hele tatt, må det gjennomføres ytterligere beregninger på det absolutte intensitetstapet før man kan trekke noen endelige konklusjoner. Hvis det viser seg at energitapet er på høyde med det som ga forverrede rekonstruksjonsresultater i denne masteroppgaven, dvs. fra og med 30%, bør det gjennomføres forsøk hvor man måler det nøyaktige forholdet mellom intensiteten til den innkommende og den spredte strålen for å se om forholdet virkelig kan bli så stort.

PREFACE

This thesis on simulations within the field of X-ray imaging concludes my five year journey on NTNU's nanotechnology program. The work has been performed within the ICONIC project, led by my supervisor Basab Chattopadhyay, for the X-ray physics group at NTNU, led by my co-supervisor Dag Werner Breiby. The thesis is a continuation of the project work performed during the autumn of 2022 [49][1]. Parts of the thesis will therefore include sections that are equal or similar to those in the project work. This will especially be the case for the motivation of the project, Chapter 1, but also the parts explaining the necessary theory to perform the simulations, Chapter 2 and 3. Some experimental details, listed in Chapter 4, will also be the same, as a goal of this thesis has been to compare the results in the aforementioned project work with the new results obtained during this spring. In the project work it was found that a large amount of scattering due to sub-resolution structures could lead to a significant degradation in the reconstruction quality obtained from a CDI experiment. This thesis has therefore been built on two main pillars. The first has been to find the scattered intensity as a function of the angular deviation from the Bragg condition for a set of scattering planes in a simulated model system of aragonite. The second has been to use this new information to see if the negative impact of Bragg scattering on the phase retrieval process in CDI could still be observed.

I would like to wrap up this preface by giving a big round of applause to all the brilliant people I've met during my years in Trondheim. A special thanks goes to all the fantastic people in my class which have made these five years pass as if it was a vacation that was simply too short.

A thanks also goes to Dag Werner Breiby and the PhD candidates in the X-ray group for their support and feedback during our biweekly meetings. This also applies for Yuriy Chushkin at the ESRF and Ragnvald Mathiesen in the X-ray group for their insightful comments throughout the year. Alain Gibaud at Le Mans University and Vincent Favre-Nicolin at the ESRF also deserve a thanks for their help during the project work.

Finally, I would like to express my gratitude to my supervisor Basab Chattopadhyay for his patience over the last year. Few others could have handled a masters student this chaotic as elegantly as you.

Finally - for real this time - I would like to thank my family for always being there, and for providing me with enough eggs, bread and love to survive the longest winters.

May you all live long and happy lives!

1 The full text can be found at https://github.com/SigurdStene. The main results will be recapitulated in Section 3.5 of this thesis.

CONTENTS

1 MOTIVATION

The ability to study the structure of materials is important to our understanding of their function. Be it a crack in a bridge, a pore in a biological sample or the morphology of nanoparticles, all structural information helps us understand how materials function and how one can alter them to have more desired properties.

X-ray microscopy techniques allow for high-resolution, three-dimensional imaging of samples ranging from viruses and integrated circuits to human organs [15, 29, 52]. Other microscopy techniques, such as electron microscopy and atomic force microscopy, can provide better spatial resolution, but these have other limitations, e.g. being restricted to looking at the surface or only working for thin samples. X-rays, with their relatively weak interaction with matter, can be used to nondestructively image thicker, three-dimensional samples [2].

Earlier, X-ray imaging techniques were limited by the difficulty to make good optical elements for X-rays, with the best resolutions being around 10 nm [11, 36, 45]. Newer, lensless techniques, such as Coherent Diffraction Imaging (CDI), have been developed to overcome this limitation [34, 44]. Here, the lenses are exchanged with area detectors. They measure the intensity of the scattered X-rays in the far-field Fraunhofer limit. By utilising that the diffraction pattern in the Fraunhofer limit is proportional to the square of the Fourier transform of the object's electron density, given that the incoming beam is coherent, one can reconstruct the object through an inverse Fourier transform [2]. To achieve this, one first has to retrieve the phase information which is lost in the intensity measurements. This is done by performing a so-called oversampling of the diffraction pattern and utilising well-developed phase retrieval algorithms [4–7, 10, 18–21, 24, 25, 33, 37].

This thesis will focus on CDI, first envisioned by Sayre in 1952 [47] and proved experimentally by Miao et al. in 1999 [34]. CDI was first developed to image non-crystalline samples before it later has been extended to crystalline samples [43].

In theory, the resolution in CDI experiments is only limited by the wavelength of the X-rays, typically in the order of angstroms. However, the best recorded resolution is 2 nm in two dimensions, where strongly scattering silver nanocubes were examined [51], and 5 nm in three dimensions [35]. Typically, high-resolution CDI results have a resolution around tens of nanometers [35].

In practice, it has been found that the resolution is limited by the maximal scattering vector one can measure [11]. For large scattering vectors, the signal-to-noise ratio is typically too low. Earlier, this was a problem for smaller scattering vectors as well, which partly explains the long development time from the method was envisaged in 1952. However, with the development of third and fourth-generation synchrotron facilities, the brightness of the X-ray beam has improved significantly.

Today's fourth-generation synchrotron facilities, such as the European Synchrotron Radiation Facility in Grenoble, France, can produce X-ray beams 10 trillion times brighter than medical X-rays [42]. This has been vital for the development of CDI and related methods. Both to achieve the required signal-to-noise ratio and also to produce an X-ray beam of well-defined coherence, which makes it possible to keep the phase information between all the constituents in the diffraction experiment [53].

A limitation of the original CDI technique is that the entire sample must be illuminated by the X-ray beam, limiting the possible samples to micrometre-sized objects due to the finite size of the beam. Newer techniques, such as ptychographic CDI [44], can image extended objects by piecing together scans taken of overlapping parts of the sample [41]. These tech-

niques do however not have the same resolution as CDI. There also exist a wide variety of other CDI-based techniques, such as Bragg CDI [58], which can be used to recover the strain structure of nanocrystals, and reflection CDI, where a surface can be studied with a sub-nanometer resolution [35].

One issue regarding CDI is that it assumes that all the intensity from the incoming beam will hit the detector in the small angle geometry. This is however not the case, as is readily measured in today's experiments, where wide-angle detectors pick up a strong signal for crystalline samples [58]. In other words, Bragg scattering due to sub-resolution structures, will reduce the intensity in the diffraction pattern for certain projections.

The effect of such intensity reductions was studied in a project work performed by the author during the autumn of 2022 [49]. It was found that Bragg scattering could have a significant negative impact on the reconstruction quality of an object, given that the intensity reduction was sufficiently large.

This thesis aims to further explore the effects of Bragg scattering and to calculate a suitable intensity reduction for a given model system of aragonite. By understanding these effects, a future goal would be to incorporate them into phase retrieval algorithms to further improve the imaging capabilities of CDI.

The intensity reduction calculations will be done numerically by simulating the diffraction pattern of an aragonite crystallite using elementary scattering equations. A rocking curve analysis will be performed around the Bragg condition for the examined scattering planes. This will to a first approximation yield information about the amount of scattered intensity for each rotation of the crystallite and the angular range over which one can measure a significant scattered signal. The methodology will be further explained in Chapter 4. First, the necessary X-ray scattering theory will be given in Chapter 2, before an introduction to CDI will be given in Chapter 3.

2 BACKGROUND INFORMATION

2.1 INTRODUCTION

The information in Section 2.1 and 2.2 has been collected from [2] if not otherwise stated. The text in these sections is partly copied from a previous work performed by the author [49]. Some subsections have been added, others have been extended, while some remain the same as in [49].

X-rays are highly energetic electromagnetic radiation. They typically have an energy ranging from 100 eV to 100 keV, which corresponds to wavelengths between 0.01 nm and 10 nm, as illustrated in Figure 1. This range includes the size of atoms and the distances between them in condensed matter. Compared to other probes, such as electrons and neutrons, X-rays interact relatively weakly with most materials, resulting in a comparably large penetration depth. This combination makes X-rays an excellent candidate to study the three-dimensional structure of materials.

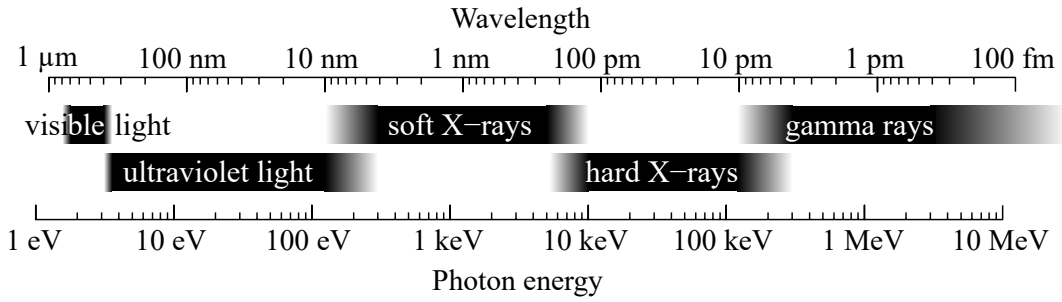

Figure 1: A comparison of the energy and wavelengths of X-rays and other types of electromagnetic radiation. X-rays cover the part of the spectrum equal to both atomic and mesoscopic structures. Adapted from Wikimedia Commons.

Structural information can be found by looking at both the absorption and scattering of X-rays. The absorption techniques utilise that the absorption of X-rays scales as Z^4, where Z is the atomic number. Hence, a contrast between different elements can be found, which can be used to study the composition of the material. This contrast is utilised in standard X-ray scans as well as in Computed Tomography, techniques which are routinely used to study the internal structure of the human body. A further discussion on absorption techniques is however out of scope for this thesis, as the focus will be on X-ray scattering techniques. Coherent X-ray diffraction imaging (CDI) is one of these techniques and will be thoroughly discussed in Chapter 3, but first, an introduction to the general X-ray scattering theory is necessary, both to facilitate the scattering calculations performed in this thesis and to understand the underlying principles of CDI.

2.2 X-RAY SCATTERING

Classically, the scattering of X-rays can be described as the interaction between an alternating electromagnetic field and electric charges. An incoming X-ray, which is an alternating electromagnetic field, will accelerate an electron and a new spherical X-ray will be produced, which will have the same wavelength as the incoming X-ray. A quantum mechanical derivation will show that X-ray scattering can be both elastic and inelastic. However, for

the material and photon energy considered in the calculations in this thesis, i.e. $CaCO_3$ and 8.051 keV, the inelastic scattering is weak. Therefore, the scattering is assumed to be fully elastic in the following derivations. At this point, it is important to note that the protons of a material will be affected by the X-rays as well, but since their mass is more than 3 orders of magnitude larger than the electrons' mass, they will not be accelerated in the same manner, and the effect will be significantly weaker than for the electrons and can thus be ignored.

When deciding the structure of materials, one must use the information available from the scattering experiment, i.e. the intensity of the scattered X-rays for each solid angle. This information is contained in the differential scattering cross-section, which is the probability that an incoming X-ray will be scattered in a certain direction, given by the solid angle. The differential cross-section can be written as

$$\frac{d\sigma}{d\Omega} = \frac{I_{sc}}{\Phi_0 \Delta\Omega'}, \tag{1}$$

where I_{sc} is the scattered intensity, Φ_0 is the incident flux and $\Delta\Omega$ is the solid angle which the detector covers. As will be shown below, this expression is strongly related to the structure of the material. By utilising this information in different ways, one can find both the atomic structure of crystals as well as the morphology of suspended particles.

Before looking at the different ways of exploiting the information contained in the differential cross-section, it is important to understand how it is related to the structure of the material. The first thing one must understand is the scattering by a single electron, before building on this to arrive at the differential cross-section of the whole material.

2.2.1 *Scattering from one electron*

By assuming an incoming plane wave and a spherical scattered wave, the differential cross section of an electron can be shown to be

$$\frac{d\sigma}{d\Omega} = \left(\frac{e^2}{4\pi\epsilon_0 mc^2}\right)^2 |\hat{\mathbf{p}} \cdot \hat{\mathbf{p}}'|^2 = r_0^2 |\hat{\mathbf{p}} \cdot \hat{\mathbf{p}}'|^2, \tag{2}$$

where $r_0 = 2.82 \times 10^{-5}$ Å is the Thomson scattering length, also known as the classical electron radius, $\hat{\mathbf{p}}$ and $\hat{\mathbf{p}}'$ are the polarisation of the incoming and scattered wave, respectively. The last term is often abbreviated P, short for polarisation factor. This factor depends on the experimental setup, and can easily be set to one in a CDI experiment.

The scattering length, also known as the scattering amplitude, is the square root of the differential cross-section. A large value for the scattering amplitude will result in a large value for the differential cross-section, i.e. a large probability of the incoming X-rays being scattered. Therefore, the scattering amplitude is also a measure of how strongly the material scatters X-rays.

2.2.2 *Scattering from one atom*

When finding the scattering amplitude of an atom, one must sum over the scattering amplitude for all the electrons, but also take into account the phase difference of the scattered X-rays arising from the difference in the electron's positions. The scattering length of an atom is defined as

$$-r_0 f^0(\mathbf{q}), \tag{3}$$

where $f^0(\mathbf{q})$ is the atomic form factor and $\mathbf{q} = \mathbf{k}' - \mathbf{k}$ is the scattering vector, where $\mathbf{k}$ is the incoming wave vector and $\mathbf{k}'$ is the wave vector of the scattered wave. The minus sign

in (3) is due to the 180° phase shift between the incoming and scattered waves. Assuming that the scattering is fully elastic, $|\mathbf{k}| = |\mathbf{k}'| = k = 2\pi/\lambda$, where λ is the wavelength of the X-rays. Then, the relation $|\mathbf{q}| = 2k\sin(\theta)$ will also be valid. Here, 2θ is the angle between the incoming and outgoing scattering vector in the scattering plane, see Figure 2.

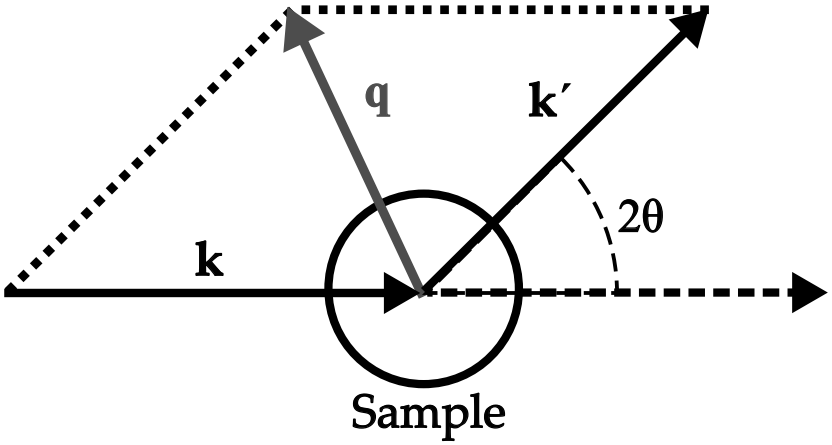

Figure 2: The relation between the scattering vector, $\mathbf{q}$, and the incoming and scattered wave vector, $\mathbf{k}$ and $\mathbf{k}'$. It is clear that $\mathbf{q} = \mathbf{k}' - \mathbf{k}$ and $q = 2k\sin(\theta)$.

The form factor in Equation (3) is defined as

$$f^0(\mathbf{q}) = \int \rho(\mathbf{x}) e^{-i\mathbf{q}\cdot\mathbf{x}} d\mathbf{x}, \tag{4}$$

where $\rho(\mathbf{x})$ is the electron density of the atom. The form factor is thus dependent on the atomic number, where a larger atomic number means more electrons and typically a larger form factor. In other words, heavy elements are stronger scatterers than light elements.

2.2.2.1 *Numerical representation of the atomic form factor*

As evident from Equation (4), the atomic form factor is the Fourier transform of the atom's electron density. The electron density can be represented as

$$\rho(\mathbf{x}) = \Psi(\mathbf{x})^* \Psi(\mathbf{x}) = |\Psi(\mathbf{x})|^2, \tag{5}$$

where Ψ is the atom's wave function [26]. The wave functions can be found by solving the Schrödinger equation using the Hartree-Fock approximation [50], or more accurately by solving the relativistic Dirac equation using Slater's $\rho^{(1/3)}$ method [32]. For the lighter elements, the Hartree-Fock description will often be sufficient, but for heavier elements, the relativistic effects cannot be neglected [32].

The simplest atomic wave function is that of hydrogen. Its ground state wave function is given by

$$\Psi_0(r) = \frac{1}{\sqrt{(\pi a_0^3)}} e^{-r/a_0}, \tag{6}$$

where r is the distance from the centre of the atom and $a_0 = 0.529$ Å is the Bohr radius [26]. Hence, the electron density is given by

$$\rho(r) = |\Psi_0(r)|^2 = \frac{1}{\pi a_0^3} e^{-2r/a_0}. \tag{7}$$

This electron density results in the following atomic form factor

$$f^0(q) = \mathcal{F}\{\rho(r)\} = \frac{1}{(1 + (\pi a_0 q)^2)^2} = \frac{1}{(1 + (4\pi^2 a_0 \sin(\theta)/\lambda)^2)^2}, \tag{8}$$

where the relations $q = 2k\sin(\theta)$ and $k = 2\pi/\lambda$ have been utilised.

The atomic form factor for other elements can be calculated in a similar manner, but the wave functions are more complicated [26]. It has therefore been made a significant effort to find a simple numerical representation of the atomic form factors [14]. One such representation is the Cromer-Mann coefficients. These are a set of nine coefficients, a_1, a_2, a_3, a_4, b_1, b_2, b_3, b_4 and c, which are used to calculate the atomic form factor as

$$f^0(\sin(\theta)/\lambda) = \sum_{i=1}^{4} a_i e^{-b_i(\sin(\theta)/\lambda)^2} + c. \tag{9}$$

This numerical representation is a good approximation for the atomic form factor of most elements and common ions as long as $\sin(\theta)/\lambda < 2\,\text{Å}^{-1}$ [14]. A comparison of the analytical and the numerical representation of hydrogen's atomic form factor is given in Figure 3. Other numerical representations which are suitable for $2\,\text{Å}^{-1} < \sin(\theta)/\lambda < 6\,\text{Å}^{-1}$ are available [22], but for the energies considered in this thesis, i.e. an incoming beam of approximately 8 keV, corresponding to a wavelength of approximately 1.5 Å, this ratio will never be larger than $2\,\text{Å}^{-1}$.

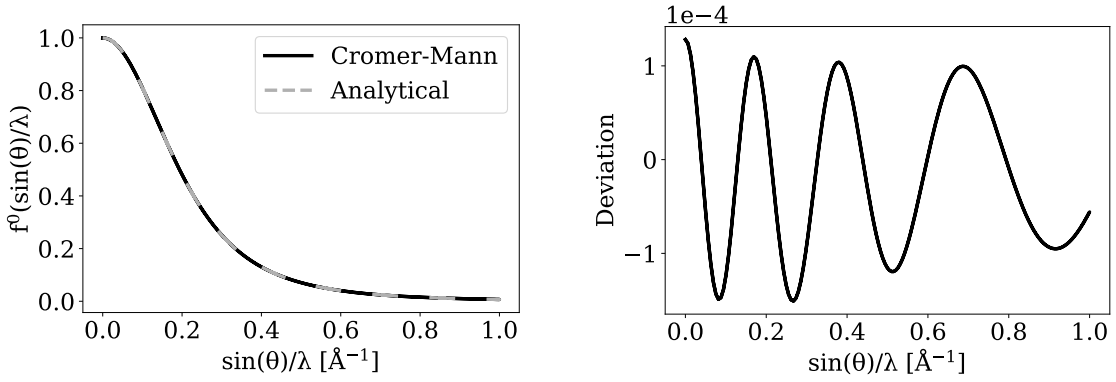

(a) (b)

Figure 3: The atomic form factor of hydrogen, both the analytical expression and the Cromer-Mann approximation, is plotted in (a). The functions overlap almost exactly, making it difficult to separate them. The largest relative deviation is less than 1.5×10^{-4}, demonstrating the good agreement between them. The deviation is given in (b). It should be noted that using the Cromer-Mann coefficients to calculate the atomic form factor of hydrogen is not necessary, as the analytical expression is simple enough to be used directly.

2.2.2.2 *Dispersion corrections for the atomic form factors*

When saying that the atomic form factor is equal to the Fourier transform of the electron density, it has been assumed that the atom is perfectly non-absorbing and that the scattering is fully elastic. Additionally, the Cromer-Mann coefficients representation assumes a spherical charge distribution. Neither of these are true for real atoms. Therefore, the atomic form factor must be corrected [8]. This is done by adding two dispersion corrections, the dispersive $\Delta f'$ and the absorptive $\Delta f''$, to f^0, such that the total form factor is given by

$$f(\mathbf{q}, \hbar\omega) = f^0(\mathbf{q}) + \Delta f'(\hbar\omega) + i\Delta f''(\hbar\omega), \tag{10}$$

where i is the imaginary unit. These corrections are known as the anomalous dispersion corrections, or the Hönl corrections [8, 55]. Like f^0, $\Delta f'$ and $\Delta f''$ are also calculated from the relativistic Dirac-Slater wave functions. A detailed explanation is given in [13]. Their values are tabulated, e.g. in [46]. They are typically small compared to f^0, but become significant

near the atoms' absorption edges. The dispersion corrections have a weak dependence on the scattering angle [55]. However, this small contribution will be neglected in this thesis. All the dispersion-related scattering effects are captured in these constants, so by exchanging f^0 with f in Equation (3), the dispersion effects will be accounted for.

2.2.3 *Scattering from larger structures*

When multiple atoms are present, the scattering amplitude is given by

$$F^{molecule}(\mathbf{q}) = -r_0 \sum_j f_j(\mathbf{q}) e^{-i\mathbf{q}\cdot\mathbf{x}_j}, \tag{11}$$

where $-r_0 f_j(\mathbf{q})$ is the scattering length of the jth atom, $\mathbf{x}_j$ is the position of the jth atom. Here, molecule simply means that there are multiple atoms present. It is thus a general term, which might include larger structures not normally considered as molecules.

When deriving this equation, it has been assumed that the incoming intensity will be the same for every scatterer and that all the scattering events are independent of each other. This is the so-called weak scattering limit, and it is the basis of the kinematical scattering theory, one of two main theories describing X-ray scattering. The other, known as the dynamical scattering theory, accounts for the possibility of multiple scattering events per photon. This is necessary for large crystals. Otherwise, the simpler kinematical theory is sufficient. This thesis will focus on kinematical scattering, since the system of interest consists of small crystallites. Therefore, the kinematical approximation will be assumed in all the following derivations.

The scattering intensity, I_{sc}, which is what one measures in a diffraction experiment, can be shown to be proportional to the absolute square of the scattering amplitude, i.e.

$$I_{sc}(\mathbf{q}) \propto \left|F^{molecule}(\mathbf{q})\right|^2. \tag{12}$$

This follows from the differential cross section being equal to the absolute square of the scattering amplitude, and the scattered intensity being proportional to the differential cross section, see Equation (1).

Since the atomic form factor is essentially the Fourier transform of the atom's electron density, the scattering intensity will be related to the Fourier transform of the object's electron density as well. This will prove important for the implementation of CDI. A short summary of the Fourier transform and its properties will therefore be given in the next section.

2.2.4 *The Fourier transform*

The Fourier transform is a mathematical operation that transforms a function from the time domain to the frequency domain, or equivalently from the space domain to the spatial frequency domain [54]. In this work, only spatial frequencies will be considered, and the Fourier transform will be denoted by $\mathcal{F}$. The Fourier transform of a function $f(\mathbf{x})$ is defined as

$$\mathcal{F}\{f(\mathbf{x})\} = F(\mathbf{q}) = \frac{1}{(\sqrt{2\pi})^D} \int f(\mathbf{x}) e^{-i\mathbf{x}\mathbf{q}} d\mathbf{x}, \tag{13}$$

where $\mathbf{q}$ is the spatial frequency vector, D is the dimension of the system considered and the integration is done over the entire space [54]. Equivalently, the inverse Fourier transform is defined as

$$\mathcal{F}^{-1}\{F(\mathbf{q})\} = f(\mathbf{x}) = \frac{1}{(\sqrt{2\pi})^D} \int F(\mathbf{q}) e^{i\mathbf{x}\cdot\mathbf{q}} d\mathbf{q}. \tag{14}$$

When calculating the Fourier transform of an object function $o(\mathbf{x})$, the resulting Fourier space quantity $O(\mathbf{q})$ can be divided into two parts as shown below

$$O(\mathbf{q}) = |O(\mathbf{q})|e^{i\Phi(\mathbf{q})}, \tag{15}$$

where $|O(\mathbf{q})|$ is the amplitude, also known as the modulus, and $\Phi(\mathbf{q})$ is the phase of $O(\mathbf{q})$ [54]. Looking back at Equation (12), it can be seen that the scattering intensity is related to the squared modulus of an object's electron density. In other words, a scattering experiment will only yield information about the amplitude, and not the phase. This is known as the phase problem of crystallography and will be further discussed in Section 3.2.

In this thesis, a numerical implementation of the Fourier transform, known as the fast Fourier transform (FFT), will be used. FFT is a numerical algorithm that computes the discrete Fourier transform (DFT) of a function, in $O(n \log n)$ time, where n is the number of data points. The DFT in one dimension is defined as

$$F_k = \sum_{n=0}^{N-1} f_n e^{-i\frac{2\pi}{N}kn}, \tag{16}$$

where N is the number of data points, f_n is the nth data point, and F_k is the kth frequency component [54]. The inverse DFT is defined as

$$f_n = \frac{1}{N}\sum_{k=0}^{N-1} F_k e^{i\frac{2\pi}{N}kn}. \tag{17}$$

Both of these will prove important when implementing the reconstruction algorithms commonly used in CDI experiments.

2.2.4.1 *Properties of the Fourier Transform*

Before proceeding with further scattering theory, some important properties of the Fourier transform will be listed, see [54] for a detailed explanation. These properties will be discussed further when they become relevant in the later sections.

1. The Fourier transform is linear:

$$\mathcal{F}\{Af(\mathbf{x}) + Bg(\mathbf{x})\} = A\mathcal{F}\{f(\mathbf{x})\} + B\mathcal{F}\{g(\mathbf{x})\}. \tag{18}$$

2. The Fourier transform of a shifted function is the same as the Fourier transform of the original function, multiplied by a phase factor:

$$\mathcal{F}\{f(\mathbf{x}+\mathbf{b})\} = e^{-i\mathbf{q}\cdot\mathbf{b}}\mathcal{F}\{f(\mathbf{x})\}. \tag{19}$$

3. The Fourier transform of a real function is symmetric around the origin:

$$\mathcal{F}\{f(\mathbf{x})\} = \mathcal{F}\{f^*(-\mathbf{x})\} = F(\mathbf{q}), \tag{20}$$

   where $f^*(\mathbf{x})$ is the complex conjugate of $f(\mathbf{x})$. For real functions, $f^*(\mathbf{x}) = f(\mathbf{x})$.

4. The Fourier transform of a convolution between two functions is the product of the Fourier transforms of the functions:

$$\mathcal{F}\{f(\mathbf{x}) * g(\mathbf{x})\} = \mathcal{F}\{f(\mathbf{x})\}\mathcal{F}\{g(\mathbf{x})\} = F(\mathbf{q})G(\mathbf{q}). \tag{21}$$

2.2.5 *Scattering from crystalline samples*

For crystalline samples, the expression in Equation (11) can be simplified by utilising that the sample consists of many repeating units known as the unit cell. This repetition might be seen as a convolution between the lattice points and the unit cell, as illustrated in Figure 4. The unit cell is described by the three vectors $\mathbf{a}_1$, $\mathbf{a}_2$ and $\mathbf{a}_3$. Hence, the position of each atom in the crystal can be described by $\mathbf{R}+\mathbf{r}$, where $\mathbf{R} = n_1\mathbf{a}_1 + n_2\mathbf{a}_2 + n_3\mathbf{a}_3$ describes which unit cell the atom is located in and $\mathbf{r}$ represents the atom's position within the unit cell. Summarised, the scattering amplitude of a crystal can be represented as

$$\begin{aligned} F^{\text{crystal}}(\mathbf{Q},\hbar\omega) &= r_0 \sum_{\mathbf{R}_n,\,\mathbf{r}_j}^{\text{All atoms}} f_j(\mathbf{Q},\hbar\omega) e^{i\mathbf{Q}\cdot(\mathbf{R}_n+\mathbf{r}_j)} \\ &= \sum_n^N e^{i\mathbf{Q}\cdot\mathbf{R}_n} \sum_j r_0 f_j(\mathbf{Q},\hbar\omega) e^{i\mathbf{Q}\cdot\mathbf{r}_j} \\ &= S_N(\mathbf{Q}) F^{uc}(\mathbf{Q}), \end{aligned} \tag{22}$$

where N is the number of unit cells, $S_N(\mathbf{Q})$ is the lattice sum and $F^{uc}(\mathbf{Q})$ is the unit cell structure factor[1]. In other words, since the electron density can be viewed as a convolution of two functions, its Fourier transform, i.e. the scattering amplitude, can be represented as the product of the Fourier transform of the two functions, as expected from Equation (21).

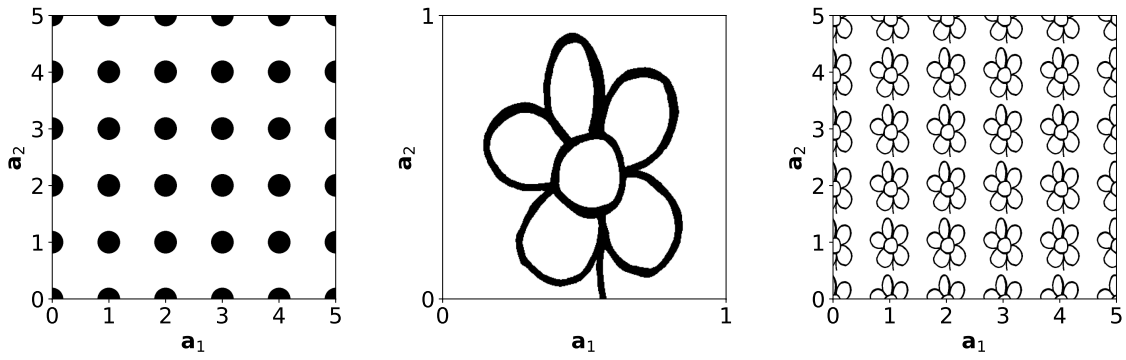

(a) Lattice (b) Basis (c) Crystal

Figure 4: A crystal can be seen as a convolution of the lattice points and a basis. Here exemplified with a small two-dimensional lattice and a flower as the basis, drawn in (a) and (b), respectively. The resulting convolution, i.e. the crystal, is drawn in (c). Note the different scales of the images.

Related to a crystal lattice is the so-called reciprocal lattice. This might be seen as a Fourier transform of the crystal lattice and is described by the reciprocal lattice points $\mathbf{G}_{hkl} = h\mathbf{a}_1^* + k\mathbf{a}_2^* + l\mathbf{a}_3^*$, with the defining property that $\mathbf{a}_i \cdot \mathbf{a}_j^* = 2\pi\delta_{ij}$, where δ_{ij} is the Kronecker delta, and hence $\mathbf{G}_{hkl}\cdot\mathbf{R} = 2n\pi$, where h, k, l and n are integers. This is achieved by defining the reciprocal vectors as

$$\mathbf{a}_i^* = 2\pi \frac{\mathbf{a}_j \times \mathbf{a}_k}{\mathbf{a}_i \cdot (\mathbf{a}_j \times \mathbf{a}_k)}. \tag{23}$$

The values h, k and l are neatly connected to the real space crystal through the Miller indices. They describe different families of planes in the crystal, and hence in the unit cell as well. The values h, k and l are chosen such that the respective family of planes cross the $\mathbf{a}_1$-, $\mathbf{a}_2$- and $\mathbf{a}_3$-axis at $\frac{i}{h}a$, $\frac{i}{k}b$, and $\frac{i}{l}c$, respectively, where i is an integer and $a = |\mathbf{a}_1|$,

1 Note that r_0 is included in the definition of F^{uc}, as opposed to the notation in e.g. [2] and [56].

$b = |\mathbf{a}_2|$ and $c = |\mathbf{a}_3|$, respectively. See Figure 5 for a two-dimensional illustration. It is easy to prove that $\mathbf{G}_{hkl}$ is perpendicular to the set of planes given by hkl

$$\begin{aligned}\left(\frac{\mathbf{a}_1}{h} - \frac{\mathbf{a}_2}{k}\right) \cdot \mathbf{G}_{hkl} &= \left(\frac{\mathbf{a}_1}{h} - \frac{\mathbf{a}_2}{k}\right) \cdot (h\mathbf{b}_1 + k\mathbf{b}_2 + l\mathbf{b}_3) = 2\pi - 2\pi = 0, \\ \left(\frac{\mathbf{a}_2}{k} - \frac{\mathbf{a}_3}{l}\right) \cdot \mathbf{G}_{hkl} &= \left(\frac{\mathbf{a}_2}{k} - \frac{\mathbf{a}_3}{l}\right) \cdot (h\mathbf{b}_1 + k\mathbf{b}_2 + l\mathbf{b}_3) = 2\pi - 2\pi = 0,\end{aligned} \tag{24}$$

where $(\mathbf{a}_1/h - \mathbf{a}_2/k)$ and $(\mathbf{a}_2/k - \mathbf{a}_3/l)$ are vectors lying in the hkl-planes [56]. Similarly, one finds that

$$d_{hkl} = \frac{2\pi}{|\mathbf{G}_{hkl}|}, \tag{25}$$

where d_{hkl} is the interplanar spacing between the hkl-planes. This relation is illustrated in Figure 5. Equation (25) exemplifies an important relation between the real and reciprocal space, namely that their length scales are inversely proportional to each other.

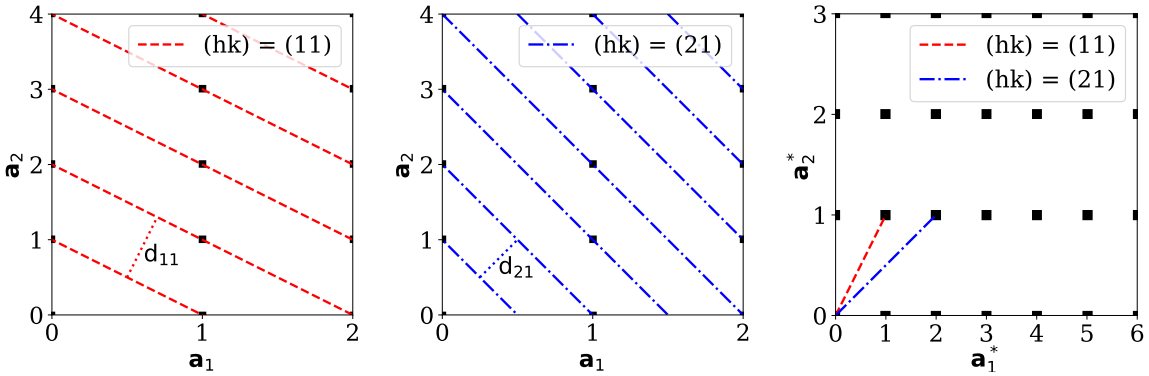

Figure 5: Two sets of scattering planes, their interplanar distances and their connection to the reciprocal lattice vectors. (a) and (b) show a two-dimensional crystal where one set of lattice planes, given by their Miller indices, is included in each figure. The square points represent the lattice points. $h = 2$ indicates that the first plane crosses the $\mathbf{a}_1$-axis at $1/2\ \mathbf{a}_1$. (c) shows the corresponding reciprocal lattice and how the normal vectors of the lattice planes are related to the reciprocal lattice vectors.

The lattice sum in Equation (22), $S(\mathbf{Q}) = \sum exp(i\mathbf{Q}\cdot\mathbf{R})$, is nothing but a three-dimensional geometrical series. To simplify, one can look at its one-dimensional equivalent. Then the sum can be expressed as

$$\sum_{n=1}^{N} e^{iQan} = \frac{\sin NaQ/2}{\sin aQ/2} e^{iQaN/2}, \tag{26}$$

Since the intensity is related to the squared modulus, it is reasonable to look at the modulus, and how it develops for large values of N.

$$|S_N(Q)| = \left|\frac{\sin NaQ/2}{\sin aQ/2}\right| \underset{N\to\infty}{=} \delta(Q - 2h\pi/a) = \delta(Q - ha^*) = \delta(Q - G_h), \tag{27}$$

where $\delta(Q - G_h)$ is the Dirac delta function, h is an integer and G_h is the one-dimensional equivalent of $\mathbf{G}_{hkl}$. By performing a similar analysis on a three-dimensional crystal, one will find the following relation

$$|S_N(\mathbf{Q})|^2 \to N v_c^* \sum_{hkl} \delta(\mathbf{Q} - \mathbf{G_{hkl}}), \tag{28}$$

where v_c^* is the volume of the reciprocal unit cell. This means that for infinitely large crystals there will only be a signal when $\mathbf{Q} = \mathbf{G_{hkl}}$. This is known as the Laue condition for diffraction, and can be visualised as an intersection between the so-called Ewald sphere and a reciprocal lattice point.

The Ewald sphere is a geometrical construct used to visualise scattering. The centre of the sphere is the initial point of the incoming wave vector, where the incoming wave vector has been placed such that it terminates at the origin of the reciprocal lattice. By allowing the scattered wave vector to start at the same initial point as the incoming wave vector, a sphere can be constructed by looking at all the possible combinations of $\mathbf{k}' - \mathbf{k}$, where the incoming wave vector is assumed to be fixed. If this sphere crosses a reciprocal lattice point, i.e. $\mathbf{Q} = \mathbf{G}_{hkl}$, there will be constructive interference, and hence a diffraction peak.

Assuming a non-divergent, monochromatic incoming beam, perfect elastic scattering and an infinitely large crystal, one would not expect to fulfil the diffraction condition. This is because both the reciprocal lattice point and the Ewald sphere would be infinitely thin, and the probability of them intersecting would essentially be equal to 0.

However, for smaller crystals, the diffraction condition is not as strict, meaning that there will be some measured intensity even when the crystal does not exactly satisfy the Laue condition. In other words, a scattering vector which deviates by a small amount ϵ from a reciprocal lattice vector will also give rise to a measurable signal, i.e. when $Q = (h + \epsilon)a^*$ for a one-dimensional crystal, then

$$|S_N((h+\epsilon)a^*)| = \left|\frac{\sin N\pi\epsilon}{\sin \pi\epsilon}\right|. \tag{29}$$

The shape of the function above defines the shape of all the diffraction peaks and is therefore also known as the shape function. Examples of $|S_N|^2$ for finite values of N are given in Figure 6.

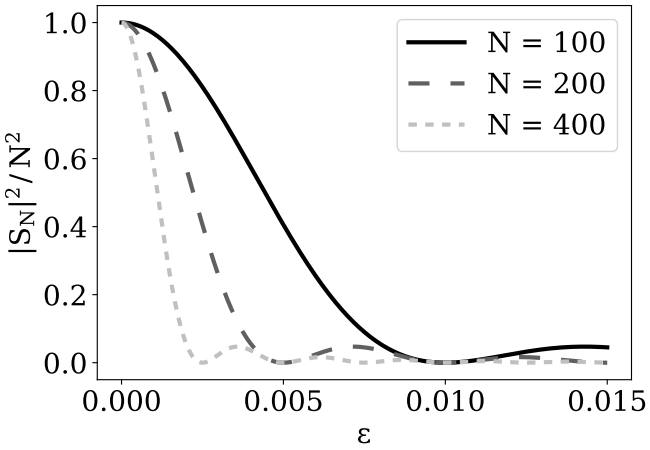

Figure 6: The absolute square of the one-dimensional lattice sum, $|S_N|^2$, plotted for three crystallite sizes, namely $N = 100$, $N = 200$ and $N = 400$, where N is the number of unit cells. The lattice sums have been normalised by dividing by their respective crystallite sizes squared. It is evident that the maximal value of $|S_N|^2$ is N^2 while the width scales as $1/N$.

When saying that the intensity will be nonzero away from the Laue condition for finite Ns, it has been assumed that $F^{u.c.}$, the unit cell structure factor, is nonzero. Generally, $F^{u.c}(\mathbf{G}_{hkl})$ can be zero, and these sets of hkl-values are known as forbidden reflections.

The Laue condition of diffraction can be shown to be equal to Bragg's law. In this thesis, the term "Bragg condition" will be used to describe the crystal being oriented such that Bragg's law is fulfilled, i.e. the normal vector of the lattice planes are parallel to the scattering plane, i.e. the xz-plane in Figure 7, and the angle between the normal vector and the incoming beam is $90° - \theta$.

2.2.6 *The amount of scattered radiation*

Ultimately, the goal of these derivations has been to decide how much of the incoming beam is scattered off the sample when it fulfils the Bragg condition, or is close to fulfilling the Bragg condition. From Equation (1) it is evident that the scattered intensity will be related to the incoming flux, the differential cross-section and the solid angle the detector covers. Warren [56] explains that[2]

$$\Phi_{sc}(\mathbf{Q}) = \Phi_0 \frac{1}{R^2} \left| F^{crystal}(\mathbf{Q}) \right|^2 = \Phi_0 \frac{1}{R^2} \frac{d\sigma}{d\Omega}(\mathbf{Q}). \tag{30}$$

Given that the reflection is not forbidden, the flux will reach a local maximum when $\mathbf{Q} = \mathbf{G}_{hkl}$. For a parallelepiped, $F^{crystal}(\mathbf{G}_{hkl})$ simplifies to $F^{uc}(\mathbf{G}_{hkl}) M_1^2 M_2^2 M_3^2$, where M_1, M_2 and M_3 are the number of unit cells along each of the parallelepiped's axes. Hence, one can write

$$(\Phi_{sc})_{max} = \Phi_0 \frac{1}{R^2} |F^{uc}(\mathbf{G}_{hkl})|^2 N^2, \tag{31}$$

where $N = M_1 M_2 M_3$.

To find the intensity, one has to integrate over the area of the detector

$$I_{sc} = \int_{Det} \Phi_{sc} dA = \Phi_0 \int_{Det} \frac{1}{R^2} \frac{d\sigma}{d\Omega} dA = \Phi_0 \int_{Det} \frac{1}{R^2} \frac{d\sigma}{d\Omega} R^2 d\Omega = \Phi_0 \int_{Det} \frac{d\sigma}{d\Omega} d\Omega, \tag{32}$$

where the integral is done over the detector. The incoming flux, Φ_0, will not depend on the detector coordinates, and can therefore be moved outside the integral. On the other hand, the scattering vector, and thus the differential cross-section will vary across the detector. In this thesis, I_{sc} is the intensity scattered off the sample for one specific sample orientation. By integrating I_{sc} over all the sample orientations close to the Bragg condition, i.e. rotating the sample in small steps around the y-axis in Figure 7, the total diffracted intensity can be found.

2.3 SCATTERING GEOMETRIES

X-ray scattering experiments can be divided into two main categories, namely wide-angle (WAXS) and small-angle scattering (SAXS), as illustrated in Figure 7. The former, which is also known as Bragg diffraction and has been the focus this far, is used to study the atomic structure of materials, while the latter is used to study the morphology. As is known from Bragg's law, the scattering angle 2θ is related to the scattering vector $\mathbf{q}$ by

$$\sin\theta = \frac{\lambda}{2d_{hkl}} = \frac{\lambda}{4\pi}|\mathbf{q}|, \tag{33}$$

From this, one can see that the scattering angle is inversely proportional to the interplanar spacing. This means that the signal registered at higher angles comes from smaller structures, while the signal at low angles comes from larger structures. At higher angles, one depends on constructive interference from the scattered waves to achieve a strong enough signal. This means that the sample has to be somewhat crystalline for the scattered waves to interfere constructively.

SAXS does not require the sample to be crystalline, and is thus more versatile in many ways. It is however not able to resolve the smallest structures in a material. Since the measurements are done at small angles, the detector is typically placed far away from the

2 Note that Warren in his derivation has used intensity as a measure of the amount of energy per unit area per unit time, while this has been defined as the flux in this thesis and the intensity has been defined as the amount of energy per unit time, following the notation found in [2].

sample to achieve a higher angular resolution. Today, one can achieve a resolution in $\mathbf{q}$ of about $1 \times 10^{-3}\,\mathrm{nm}^{-1}$ [38]. CDI is inherently a SAXS technique, but in this project, the effects, if any, of the wide-angle scattering will be studied.

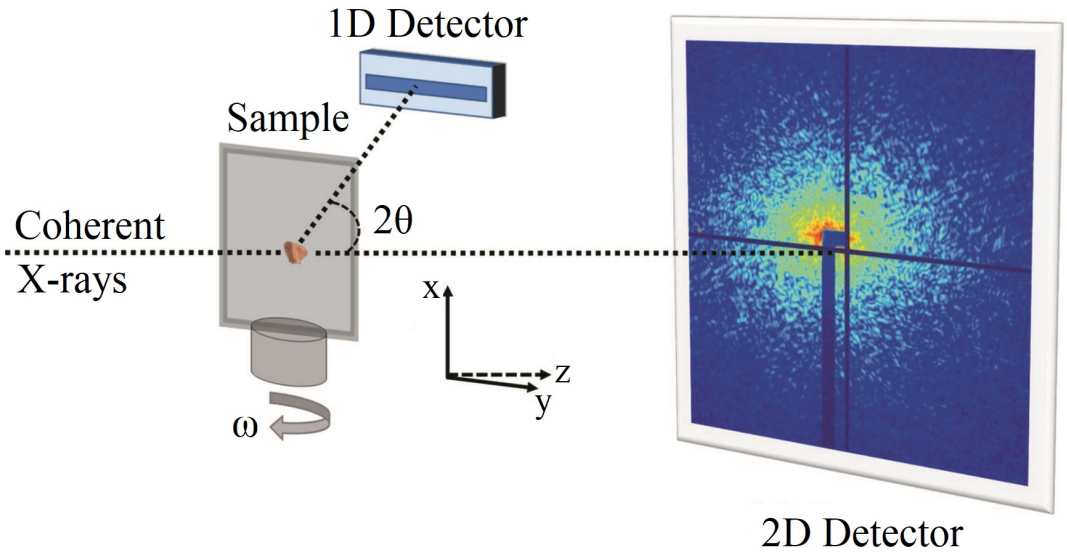

Figure 7: Illustration of the two main scattering geometries as performed in a CDI experiment. The two-dimensional detector measures the small angle scattering signal, while the one-dimensional, located at higher scattering angles, measures the wide angle signal. Adapted from [12]. The wide-angle detector can also be

2.4 X-RAY BEAM - GENERATION AND REQUIREMENTS

The information in Section 2.4.1 was collected from [59] if not otherwise stated. Likewise, most of the information in Section 2.4.2 was retrieved from [2] and [53]. Finally, Section 2.4.3 is based on all of the three aforementioned references.

2.4.1 *X-ray generation*

There are strict restrictions on the quality of X-ray beams used in CDI experiments. The X-rays utilised in CDI experiments are typically produced at synchrotron facilities, such as the European Synchrotron Radiation Facility (ESRF) in Grenoble. A synchrotron is a particle accelerator, where electrons in vacuum are accelerated to relativistic speeds and forced to follow a circular path by a magnetic field. The electrons are carried around large storage rings, the one at ESRF having a circumference of 844 m [42], and the X-ray beam generation is done in tangential insertion devices called undulators. An undulator consists of many pairs of magnets, with alternating directions of the field. By introducing the electrons to this alternating magnetic field, the electrons start to oscillate and hence accelerate, creating electromagnetic radiation with a frequency corresponding to the frequency of the oscillation, as described by Maxwell's equations. As opposed to traditional rotating anode sources, undulators will yield X-ray beams of sufficient quality to perform CDI experiments. What this means will be discussed in Section 2.4.2 and 2.4.3.

It should also be mentioned that tabletop sources which can produce electromagnetic radiation in the extreme UV- and soft X-ray range of sufficient quality to perform CDI experiments have been developed [23]. This will allow for a broader range of experiments to be performed, as the availability of beam time at synchrotron facilities is limited.

2.4.2 *Coherence*

A perfectly coherent wave is usually known as a plane wave. It is monochromatic and has a constant phase difference between different points in the wave, i.e. all the constituents of the wave travel in the same direction with the same velocity. A perfectly coherent wave is a theoretical concept not achievable in practice. Real beams are neither perfectly monochromatic nor do they propagate in one well-defined direction. One can however create beams that come close to the ideal. To put a number on the deviation from the ideal coherent wave, one can use quantities known as the longitudinal and transversal coherence length.

The longitudinal coherence length is a measure of how far two photons of slightly different wavelengths can propagate before they are out of phase, assuming they were in phase to begin with. If they're out of phase at a distance given by the longitudinal coherence length, L_L, they will be in phase again at $2L_L$. The longitudinal coherence length can be approximated to

$$L_L = \frac{\lambda^2}{2\Delta\lambda}, \tag{34}$$

where λ is the wavelength of the photons and $\Delta\lambda$ is the bandwidth of the photons. Here, $\Delta\lambda$ is assumed to be small, such that all the photons have approximately the same wavelength λ. With an incoming energy of 9 keV, having passed through a Si crystal monochromator for the (111) reflection, the longitudinal coherence length will be approximately 500 nm [61]. An illustration of the longitudinal coherence length is shown in Figure 8.

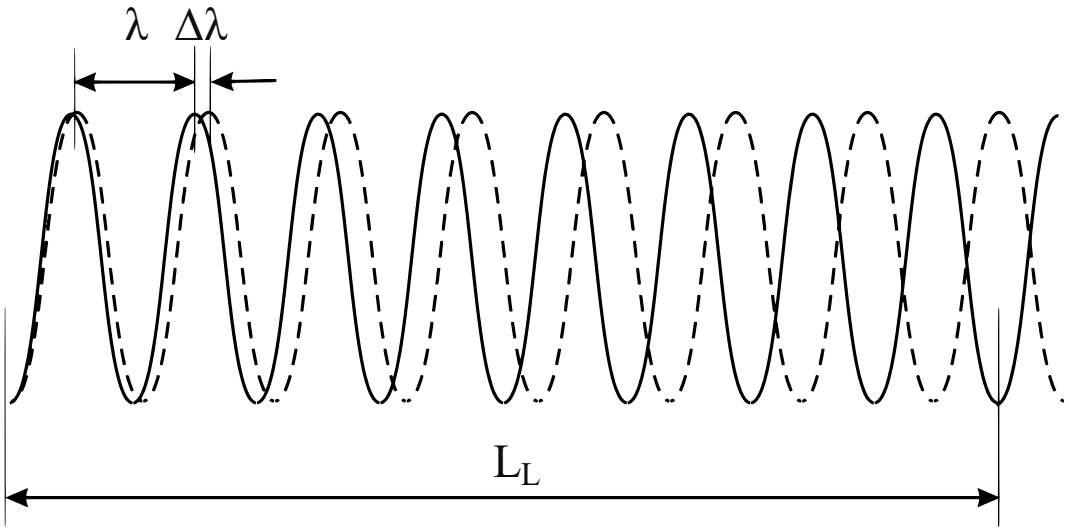

Figure 8: Illustration of the longitudinal coherence length. The two photons are in phase at $x = 0$, but out of phase at $x = L_L$. Here, $\Delta\lambda/\lambda$ is large compared to CDI experiments to highlight the effect. Illustration adapted from [53].

The transverse coherence length is a measure of how well the constituents of the beam travel in the same direction. This deviation might be caused by photons originating from different point sources. Huygens' principle says that each point in a wavefront might be seen as a point source, so any finite-sized beam will inherently have some transversal coherence length related to it. Again, if they're out of phase at a distance L_T, where L_T is the transversal coherence length, they will be in phase again at $2L_T$. The transverse coherence length is given by

$$L_T = \frac{\lambda R}{2D}, \tag{35}$$

where D is the distance between the point sources and R is the distance from the point sources to the observation point. R is assumed to be large compared to D, such that one

can use the same value for the point sources. The transverse coherence lengths at third-generation synchrotron sources are in the range of 3 to 500 µm [61], depending on their geometry. To perform coherent diffraction, the transverse coherence length has to be larger than the size of the sample.

The reason why one needs a coherent beam in CDI experiments is outlined below. From Equation (12) it can be shown that the intensity measured from a perfectly coherent beam is given by

$$I(\mathbf{q}) \propto \left| \sum_i f_i(\mathbf{q}) \right|^2 . \tag{36}$$

The intensity is thus proportional to the square of the sum of the form factors. This is due to the perfect correlation between the different constituents.

For a perfectly incoherent beam, the cross terms in the sum will be completely uncorrelated, and the intensity will be given by

$$I(\mathbf{q}) \propto \sum_i |f_i(\mathbf{q})|^2 . \tag{37}$$

The effects of this can be seen in Figure 9, where it is shown that a coherent beam will result in a so-called speckle pattern. These speckles contain information about the positions of the objects, which is lost with an incoherent beam. In other words, the diffraction intensity from an incoherent beam is the sum of the diffraction intensities from the individual parts, meaning that the final diffraction pattern is unaffected by the interplay between them.

2.4.3 *Brilliance*

In order to produce a beam of decent coherence, one must use a monochromator and apertures. The monochromator will reduce the bandwidth of the photons, resulting in a longer transversal coherence length, while the apertures will lower the divergence of the beam, hence minimising the transversal coherence length. This might result in a highly coherent beam, but the price to pay is a low intensity. By blocking out substantial parts of the beam, the intensity might end up being too low to be of any use. To overcome this, one must have a sufficiently bright source. All of these factors are important to consider when designing an X-ray beam, and they are collected in a term called brilliance, which is a measure of the quality of the beam. The brilliance is given by

$$\text{Brilliance} = \frac{\text{Photons/seconds}}{(\text{mrad})^2(\text{mm}^2 \ \text{source area})(0.1\%\text{bandwidth})}, \tag{38}$$

where the numerator is the incoming intensity of the beam, mrad is a measure of the divergence of the beam and 0.1% bandwidth is the relative bandwidth compared to 0.1% [2]. From this, one can see that a high brilliance is achieved by having a high intensity, a narrow beam with low divergence and a small bandwidth. All of which are desired properties of the beam. The reason one wants a high brilliance is that the scattering amplitudes are small for X-rays, and hence the signal-to-noise ratio can be poor, making it difficult to retrieve useful information. For third-generation synchrotron sources, the brilliance is typically 10 orders of magnitude larger than traditional rotating anode sources. This has allowed for significant progress in the field of X-ray physics over the last decades and has been crucial for the development of CDI. Fourth-generation sources, such as the ESRF, are even better, typically having a brilliance two orders of magnitude better than the third-generation sources [42].

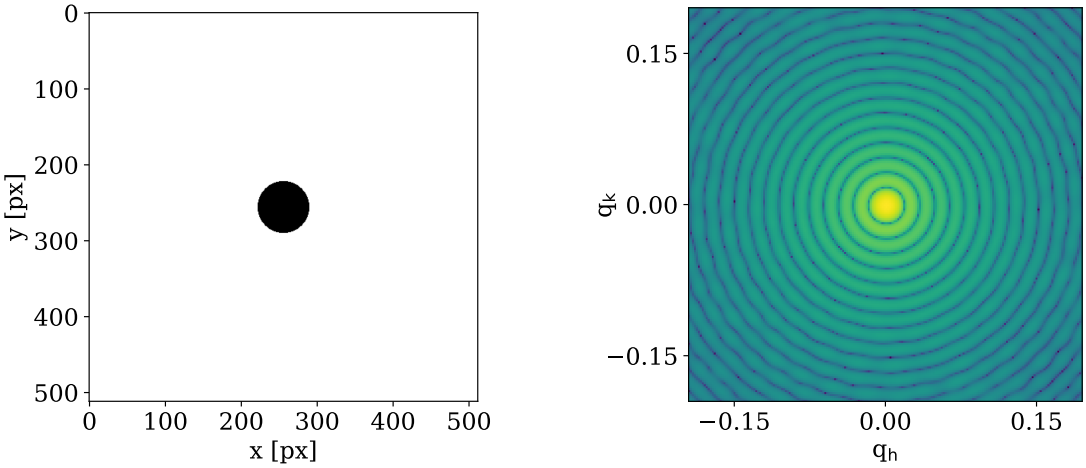

(a) One circle.

(b) Corresponding diffraction pattern.

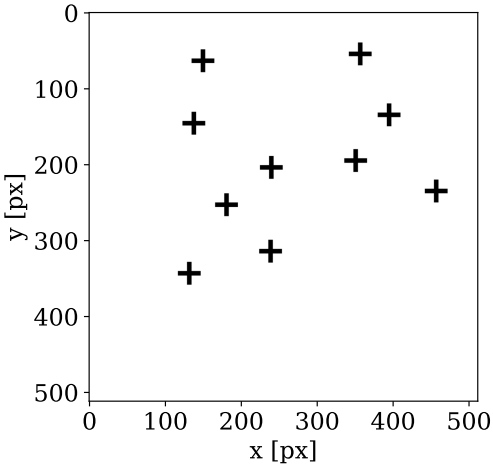

(c) The circles' centre of mass.

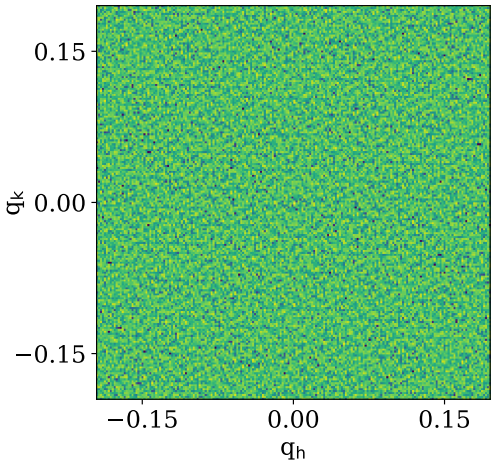

(d) Corresponding diffraction pattern.

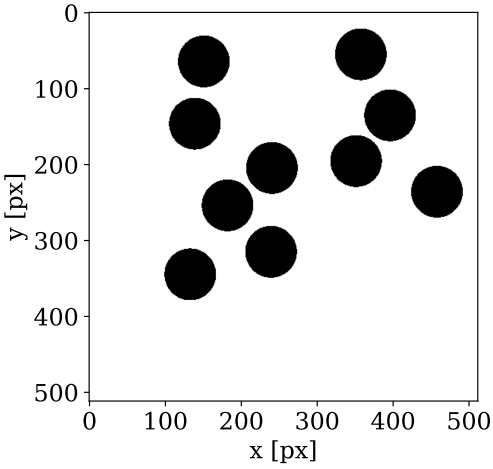

(e) All the circles.

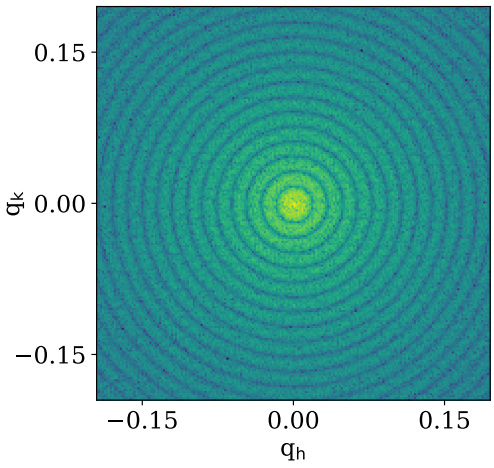

(f) Final diffraction pattern.

Figure 9: Simulated speckle pattern from 10 circles. (a), (c) and (e) show the real space objects, while (b), (d) and (f) show their respective diffraction pattern. The final real space object can be seen as a convolution of one circle and a collection of positions. Following Equation (21), the diffraction pattern in (f) should be a multiplication of the patterns in (b) and (d), which indeed is the case. If an incoherent beam had been assumed, the final diffraction pattern in (f) would be equal to the one in (b). Hence, the positional information of the circles would be lost. This is the critical information kept in the speckle pattern of (d). The circles' centre of mass are points, but are shown as crosses in Figure (c) for clarity.

3 COHERENT DIFFRACTION IMAGING

3.1 INTRODUCTION

As shown in the previous chapter, there is a close relation between the electron density of an object, $\rho(\mathbf{x})$, and the intensity of the measured diffraction pattern, namely that the scattering amplitude and therefore the measured intensity is related to the Fourier transform of the electron density. Unfortunately, one cannot simply apply an inverse Fourier transform to retrieve the electron density from the diffraction pattern, since the measured intensity will be proportional to the absolute square of the Fourier transform, hence not including the phase information. This is known as the phase problem of crystallography and will be further discussed in Section 3.2. However, what Sayre suggested in 1952 [47], and Miao et al. proved experimentally in 1999 [34], was that one could retrieve the phase information in scattering experiments by performing a so-called oversampling in Fourier-space. The theoretical proof of this was given by Bates, Fright et al. in the early 1980s [4–7], and the practical phase retrieval algorithms were developed by Fienup et al. in the 1970s [18–21, 24, 25]. The concept of oversampling will be discussed more thoroughly in Section 3.3, while the phase retrieval algorithms will be covered in Section 3.4.

3.2 PHASE PROBLEM

Before elaborating on the retrieval of the phase information through oversampling and phase retrieval algorithms, its importance will be briefly discussed. As mentioned above, and can be seen in Equation (12), the phase information is lost in the diffraction pattern. Hence, one cannot reconstruct the object through an inverse Fourier transform, even though one has all of the amplitude information.

To illustrate the importance of the phase, the Fourier transform of an image can be calculated before trying to reconstruct it by either swapping the phase or the amplitude with a random distribution, before performing the inverse Fourier transform. This will highlight how much of the information is kept in the phase, as illustrated in Figure 10 and 11. In Figure 10, the phase information has been exchanged with a random distribution. In this case, the reconstructed image does not resemble the original image in any apparent way, indicating that the amplitude information is not enough to reconstruct the image. The opposite case is shown in Figure 11, i.e. that the amplitude information has been exchanged. Here, one can see clear resemblances between the original and reconstructed image, motivating the need for a phase-retrieval process in CDI, as most of the information seems to be carried by the phase.

This has also been shown by Oppenheim and Lim [40] and by Juvells et al. [30], who argued that the phase carries the most relevant information for most images, but that the amplitude could play a more important role for images with strong geometrical markers. Since most of the information is kept in the phase, it is crucial to retrieve this information if one wishes to reconstruct the object using an inverse Fourier transform. Luckily this can be done, as will be shown in the following sections.

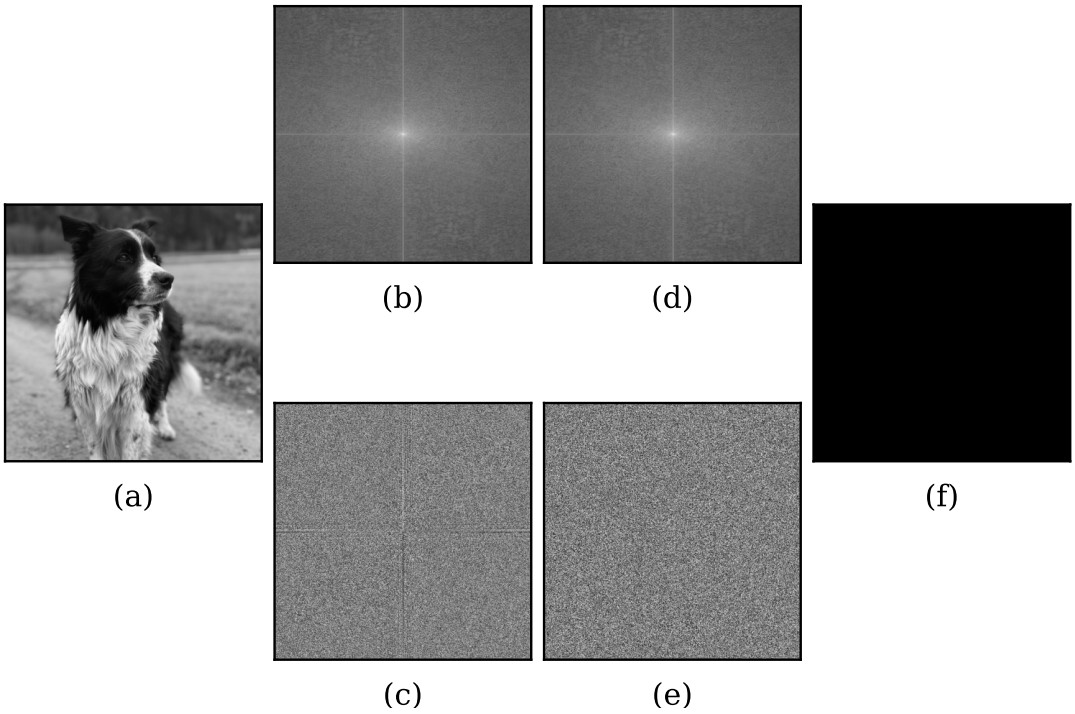

Figure 10: Reconstruction with a random phase. (a) is the original image. (b) and (c) is the amplitude and phase of the Fourier transform of the image, respectively. (d) is again the amplitude from the original image, while (e) is the average of the phase collected from an ensemble of images. (f) shows the result after performing an inverse Fourier transform with the amplitude from the original image and the random phase.

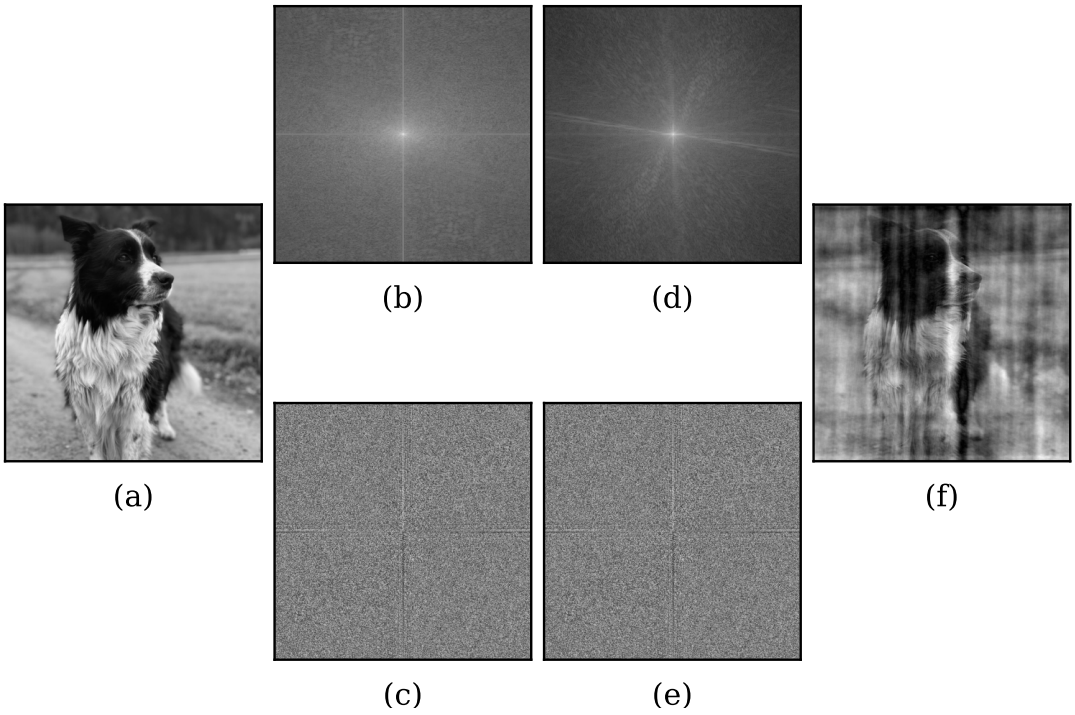

Figure 11: Reconstruction with a random amplitude. (a), (b) and (c) is the same as in Figure 10. Here, (d) is the average amplitude information from an ensemble of images, while (e) is the phase from the original image. Again, (f) is the result of an inverse Fourier transform using (d) and (e).

3.3 OVERSAMPLING

The fundamental criteria for phase retrieval is to perform a so-called oversampling in Fourier space. The oversampling criterion builds on the work of Whittaker [57], Nyquist [39] and Shannon [48], who showed that all bandlimited signals can be perfectly reconstructed if one samples them at a rate at least twice as high as the highest frequency.

For materials, this translates to sampling the diffraction pattern at a frequency finer than the crystallographic sampling. This was Sayre's key insight from 1952 [47], who said that the phase could be retrieved if one sampled at a frequency of $1/2a$, where a is the length of the unit cell. This was further elaborated by Miao et al. in 1998 [37], who showed that the oversampling criterion was not as strict as previously thought. Instead of oversampling with a factor of two in every dimension, i.e. with a factor of eight for a three-dimensional object, they showed that it is sufficient to oversample with a factor of $2^{1/D}$ in every dimension for real-valued objects, where D is the dimension of the system. For complex-valued objects, the chosen criterion was stricter, but still not as strict as previously thought.

The process of oversampling also works for non-crystalline samples. Here, one usually says that the sampling frequency should be twice as large as the Bragg density, where the Bragg density is defined as the density of Bragg peaks that would have been produced if the non-crystalline sample were turned into a crystal by repeating the structure with contact, but without overlap, in all directions [4, 37]. This equals the Bragg density of the autocorrelation function, which is what one measures in a scattering experiment. An illustration of this can be seen in Figure 12. The finer-than-Bragg criterion corresponds to oversampling the sample in real space as well [37]. This is given by the oversampling ratio, σ, defined as

$$\sigma = \frac{\text{electron density region} + \text{no-density region}}{\text{no-density region}}. \tag{39}$$

Following the discussion on the oversampling in Fourier space, it is clear that the oversampling ratio must be larger than 2 [37]. This is shown in Figure 13.

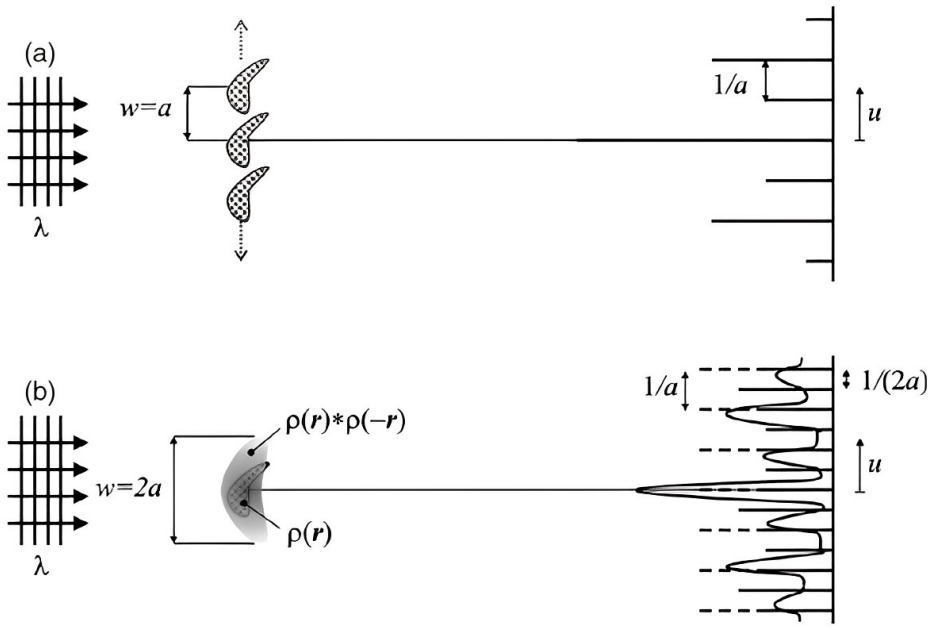

Figure 12: Illustration of the oversampling criterion. The Bragg density is given by assembling the initial structure into a perfect crystal. By sampling at a frequency twice as high as the Bragg density, equal to the Bragg density of the object's autocorrelation, one can retrieve the phase information. Adapted from [53].

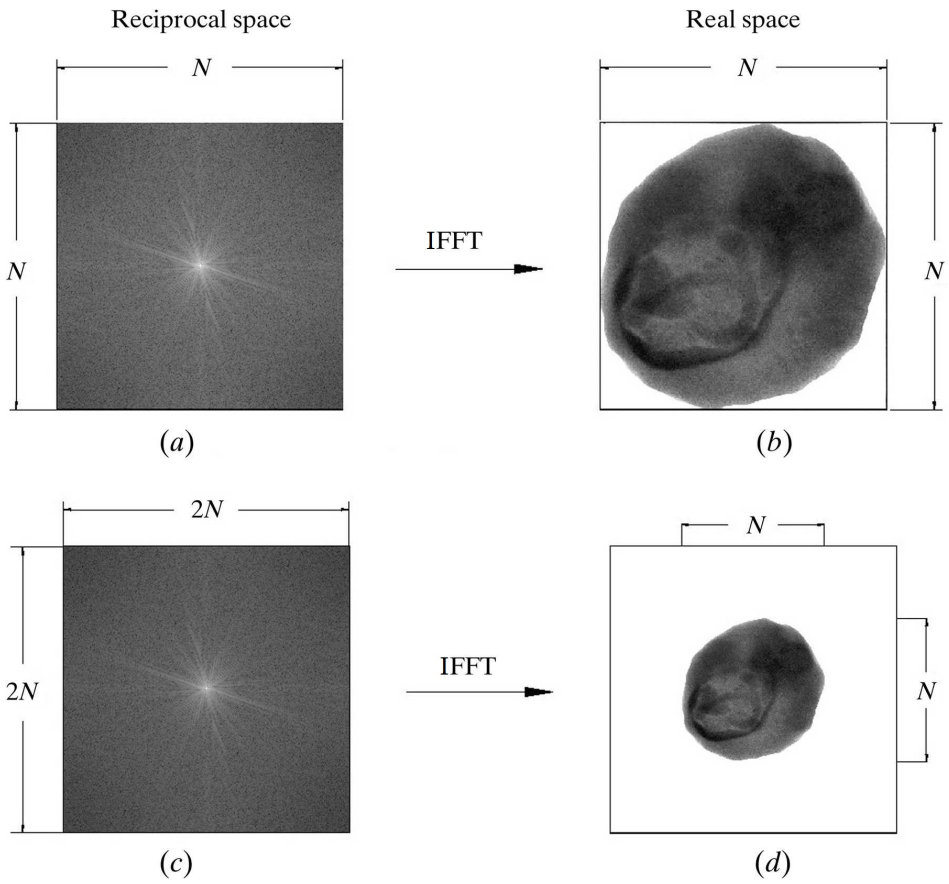

Figure 13: Illustration of how the oversampling in Fourier space corresponds to a higher oversampling ratio in real space. By sampling at twice the Bragg density, as done in (c), one will have a sufficiently large no-density area to retrieve the phase information, as shown in (d). Adapted from [37].

3.4 PHASE RETRIEVAL ALGORITHMS

As shown in Section 3.2, knowing the phase is crucial when reconstructing an object from Fourier space to real space. There are currently several algorithms available to overcome this problem. Some of the most common and easily implemented algorithms are the error reduction algorithm and the hybrid input-output algorithm [18, 19]. Both of these are iterative algorithms, where an initial guess on the phase is steadily improved to minimise the difference from the real phase. An example of a phase retrieval process can be seen in Figure 14.

In general, it should be noted that the phase retrieval algorithms are only able to decide the phase up to a constant phase factor. Adding a constant term to the phase will not change the solution, and the phase is therefore not uniquely determined. This is known as the uniqueness problem in phase retrieval. In general, if $o(\mathbf{x})$ is the actual solution, one cannot separate this from $o(\mathbf{x}+\mathbf{x_0})exp(i\phi_0)$, where ϕ_0 is a constant phase factor and $\mathbf{x_0}$ is a shift in real space. For a real-valued object, $o^*(-\mathbf{x}+\mathbf{x_0})exp(i\phi_0)$ will also be a valid solution to the phase retrieval problem. This follows from the shifting and centrosymmetric property of the Fourier transform, as described in Equation (19) and (20). $o(\mathbf{x})$, $o(\mathbf{x}+\mathbf{x_0})exp(i\phi_0)$ and $o^*(-\mathbf{x}+\mathbf{x_0})exp(i\phi_0)$ are known as the trivial characteristics of the phase problem of $o(\mathbf{x})$ [37]. They are trivial in the sense that they all represent the same object, just shifted or rotated in space. In other words, CDI is not able to retrieve the exact position or rotation of an object, but this is seldom of interest and could easily be found in other ways. One advantage of this, i.e. that CDI is not able to separate between different positions of the object, is

that CDI is unaffected by small sample vibrations during the diffraction experiment, thus making it more robust against experimental noise [35].

Apart from the trivial characteristics, it has been shown that the phase can almost always be decided uniquely for real and positive objects of dimension $D \geqslant 2$ [10, 28].

3.4.1 *Error reduction algorithm*

Fienup's error reduction algorithm (ER), which is a generalisation of the Gerchberg-Saxton algorithm originally used in electron diffraction imaging [18, 24, 25], is one of the simplest phase retrieval algorithms. It uses two constraints, one in real space and one in Fourier space, to iteratively find the phase of the object, $\Phi(\mathbf{q})$, from an initial guess, $\Phi_0(\mathbf{q})$, by performing forward and inverse Fourier transforms repetitively [18].

The first constraint is that the object lies within a volume S in real space known as the support. Additionally, the object is real and non-negative within this volume [18]. Outside this volume, the object function, $o(\mathbf{x})$, should vanish. The support can be decided by looking at the autocorrelation of the object. By using a diameter that is half the size of the largest diameter of the autocorrelation, one can ensure that the object is fully encapsulated within the support. This follows from the properties of the autocorrelation, which necessarily is at least twice as large as the object itself. The autocorrelation can easily be calculated since it is just the inverse Fourier transform of the square of the Fourier modulus, which is essentially what one measures in a diffraction experiment. This follows from Equation (21) by setting the two functions equal to each other.

$$\mathcal{F}^{-1}\left\{|\mathcal{F}\{o(\mathbf{x})\}|^2\right\} = \mathcal{F}^{-1}\left\{O(\mathbf{q})O^*(\mathbf{q})\right\} = o(\mathbf{x}) * o(-\mathbf{x}). \tag{40}$$

where the last term is the autocorrelation of the object. This is however not a very tight constraint and can lead to slower convergence [19]. Newer methods allow for an update of the support as more information about the object is found further out in the reconstruction process [33, 60]. It is also possible to use other a priori information about the object if that is available.

The second constraint, i.e. the Fourier constraint, is based on the measured intensity. When performing the forward Fourier transform, the calculated amplitude is exchanged with the measured amplitude, $|O(\mathbf{q})|$. The method is summarised below [19].

1. Choose random initial phase $\Phi_0(\mathbf{q})$, which yields $O_0 = |O(\mathbf{q})|exp(i\Phi_0(\mathbf{q}))$.
2. Perform inverse Fourier transform to estimate the object function $o(\mathbf{x})$:
$$o'_n(\mathbf{x}) = \mathcal{F}^{-1}\{|O(\mathbf{q})|exp(i\Phi_n(\mathbf{q}))\}. \tag{41}$$
3. Apply the real space constraint:
$$o_{n+1}(\mathbf{x}) = \begin{cases} o_n(\mathbf{x})' & \text{if } \mathbf{x} \in S, \\ 0 & \text{if } \mathbf{x} \notin S. \end{cases} \tag{42}$$
4. Perform Fourier transform to estimate $O(\mathbf{q})$:
$$O'_{n+1}(\mathbf{q}) = \mathcal{F}\{o_{n+1}(\mathbf{x})\}. = |O_{n+1}(\mathbf{q})|exp(i\Phi_{n+1}(\mathbf{q})). \tag{43}$$
5. Apply Fourier space constraint:
$$O_{n+1}(\mathbf{q}) = |O(\mathbf{q})|exp(i\Phi_{n+1}(\mathbf{q})). \tag{44}$$

6. Repeat Points 2, 3, 4 and 5 until convergence, i.e.

$$o_{n+1}(\mathbf{x}) = o_n(\mathbf{x}) \text{ and } |O'_n(\mathbf{q})| = |O(\mathbf{q})|. \tag{45}$$

Typically, the mean square error in Fourier space is used to determine convergence. It is defined as:

$$\epsilon_n = \frac{\int_V |O_n(\mathbf{q}) - O(\mathbf{q})|^2 d\mathbf{q}}{\int_V |O(\mathbf{q})|^2 d\mathbf{q}}, \tag{46}$$

where V is the volume of the measured reciprocal space.

It has been proven that the mean squared error between $|O_n(\mathbf{q})|$ and $|O(\mathbf{q})|$ will decrease or at worst stay the same for each iteration. This is the reason why the algorithm is called the error reduction algorithm. Typically, the error will decrease rapidly initially, before flattening out [18, 19]. Another known problem with the ER algorithm is that it usually converges to a local minimum instead of a global minimum. It might also end up in a state where the reconstructed object is a combination of the actual object and its centrosymmetric inversion, following the centrosymmetric property of the Fourier transform as described in Equation (20).

3.4.2 *Hybrid input-output algorithm*

The hybrid input-output algorithm (HIO) was developed by Fienup et al. [18] to speed up the aforementioned convergence problem of ER. HIO differs from ER by altering the real space constraint in Step 3 by using a negative feedback loop to minimise the mean square error in Fourier space. There are multiple implementations of HIO, but one common presented by Fienup [18] exchanges the real space constraint with the following:

$$f_{n+1}(\mathbf{x}) = \begin{cases} f'_n(\mathbf{x}) & \text{if } \mathbf{x} \in S, \\ f_n(\mathbf{x}) - \alpha f'_n(\mathbf{x}) & \text{if } \mathbf{x} \notin S, \end{cases} \tag{47}$$

where α is a constant that determines the amount of negative feedback. Fienup mentioned that a combination of different constraints gave the best results. Fienup also proved that HIO is fairly resilient against noise, keeping the low-frequency information intact even at relatively high noise levels.

Despite the similarities between the algorithms, HIO doesn't suffer from many of the same drawbacks as ER. However, it might have problems reaching a minimum, so one usually switches to another algorithm, such as ER, when HIO has stabilised around some value. One might also use variations of HIO, such as the detwinning HIO. In this variant, the support is halved along a direction every iteration to overcome the possible problem of centrosymmetric twins [21, 27].

3.4.3 *Shrink wrap algorithm*

As mentioned in Section 3.4.1, there exist methods to automatically update the support of the object during the reconstruction process. The shrink wrap algorithm (SW), developed by Marchesini et al. [33], is one such method. It is a modification of HIO, where the support is updated around every twentieth iteration. By updating the support, one will eventually end up with a so-called "tight support", i.e. a support that is as close to the exact object shape as possible [31]. The support is updated by thresholding, i.e. removing the outer parts of the support where the reconstructed object is below a certain value, which is often taken to be relative to the maximum value of the reconstructed object.

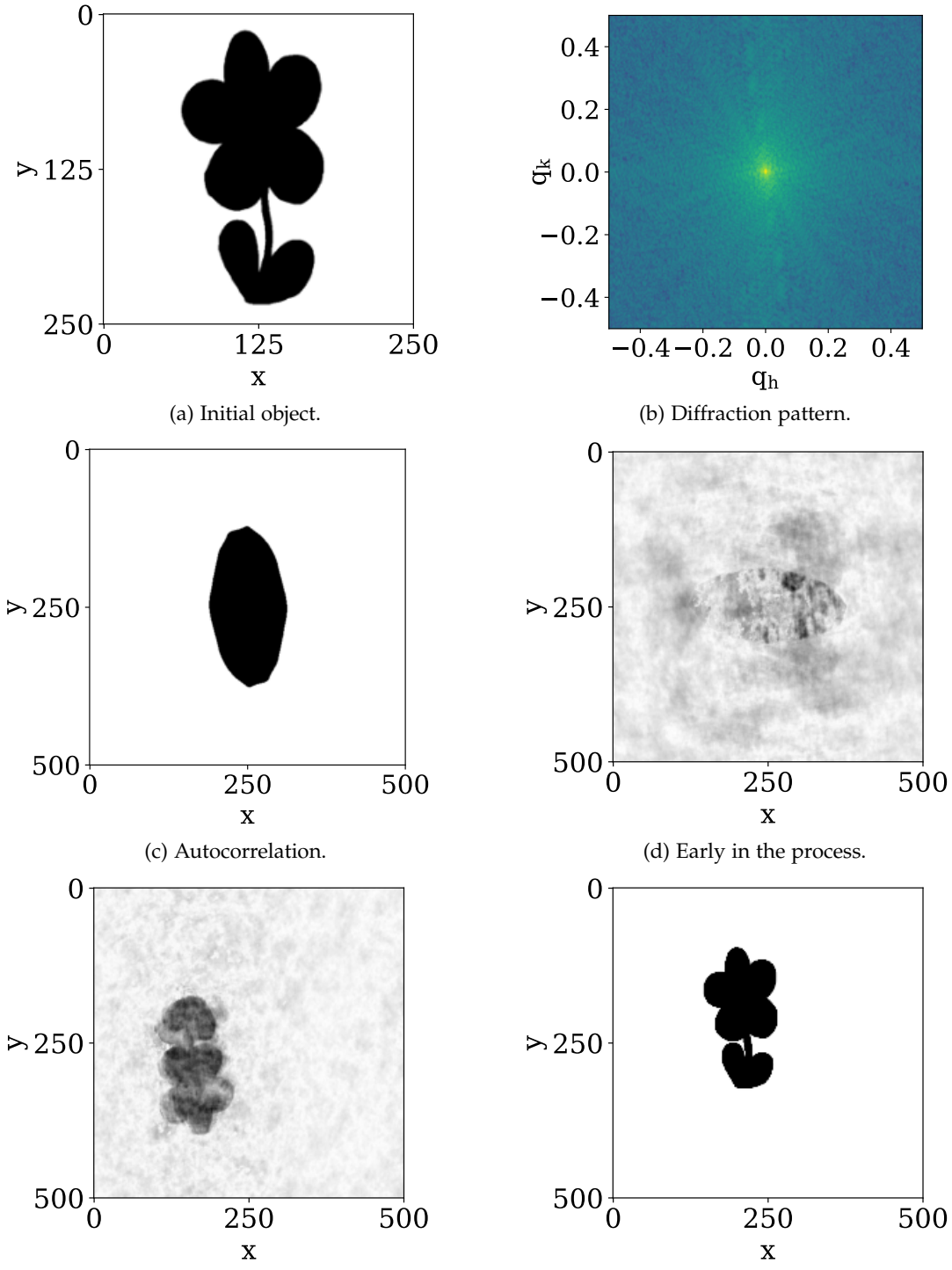

(a) Initial object.

(b) Diffraction pattern.

(c) Autocorrelation.

(d) Early in the process.

(e) Further out in the process.

(f) Final reconstruction.

Figure 14: Illustration of the reconstruction process in CDI. (a), (b) and (c) show the initial object, its diffraction pattern and its autocorrelation, which was used as the initial support, respectively. (d) shows the reconstructed object after performing 5 iterations of HIO, while (e) shows the reconstructed object after 6 shrink wrap iterations, where one shrink wrap iteration contained 20 HIO iterations followed by a support update. Lastly, the final result can be seen in (f). Here, 20 SW iterations and 20 ER iterations have been performed. The oversampling ratio was 2 in both directions, indicated by the initial matrix being twice as small as the rest. The different rotation of the object follows from the properties of the Fourier transform, as described in Section 2.2.4.1. The length scales for all the real space objects, i.e. all except (b), are given in pixels.

3.5 THE INFLUENCE OF BRAGG SCATTERING

As mentioned in Chapter 1, intensity losses due to Bragg scattering might have a negative effect on the reconstruction quality in CDI experiments. This effect was studied in a project thesis performed by the author during the autumn of 2022 [49]. A short summary of the method and the results is given below.

The effect was studied using numerical simulations. An object, shown in Figure 15, was generated and its three-dimensional diffraction pattern was calculated using the open source python package PyNX, developed by Favre-Nicolin et al.[1].

The object consisted of two intersecting ellipsoids with different densities. Their scattering amplitudes were calculated separately, using Equation (11), utilising the linear properties of the Fourier transform. An amplitude reduction filter was then applied to the scattering amplitudes of the two ellipsoids separately, each at a different angle, simulating that the ellipsoids were rotated with respect to each other. An example of a reduction filter can be seen in Figure 16. In total, 9 different intensity reductions were examined, namely 0%, 5%, 10%, 15%, 20%, 30%, 40 %, 50% and 60%.

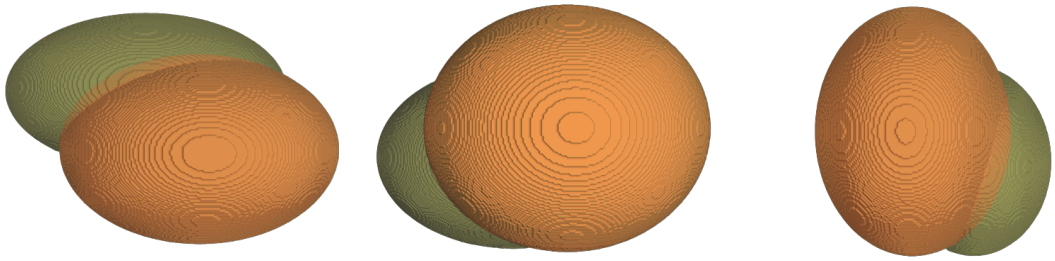

(a) The examined object viewed from the front.

(b) The examined object viewed from the bottom.

(c) The examined object rotated and viewed from the right.

Figure 15: The examined object viewed from three different directions. The orange area had a relative density of 1, while the green had a relative density of 0.8.

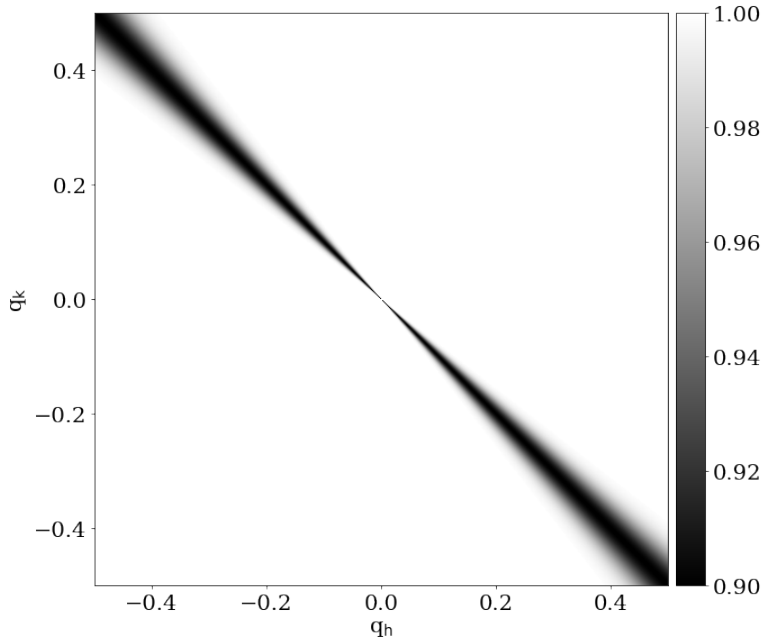

Figure 16: Illustration of a filter that was applied to the diffraction pattern to simulate the reduction in intensity due to Bragg scattering. Here, a 10% reduction would have been applied.

1 A further introduction to the package can be found in [16, 17] and at http://ftp.esrf.fr/pub/scisoft/PyNX/

The scattering amplitudes were then added together and squared to obtain the intensity of the diffraction pattern. This intensity was then used as the input for the phase retrieval algorithm. The phase retrieval algorithm was a combination of the algorithms described in Section 3.4. Both the HIO and the ER algorithms were used, as well as a support shrinking algorithm. The reconstruction itself was also performed using PyNX's implementation of the phase retrieval algorithms. Ten reconstruction were performed for each intensity reduction parameter. Subsequent postprocessing of the reconstructed objects was done to align the reconstructed objects with the original object. This was done to examine the deviation from the initial object as well as the general density distribution of the reconstructed objects. The results from these simulations are shown in Figure 17 and 18.

The results demonstrate that the intensity reductions had a negative effect on the reconstruction quality. Both the density distribution and the overall shape of the reconstructed objects were affected by the intensity reductions. For the largest intensity reductions, the reconstructed objects were qualitatively different from the original object. Therefore, it was not possible to find a reasonable average of the reconstructed objects. Hence, they are not included in Figure 18, where the deviations between the average structures and the initial object are shown. On the other hand, the differences were smaller for the weaker intensity reductions, but the negative impact on the reconstruction quality could still be seen.

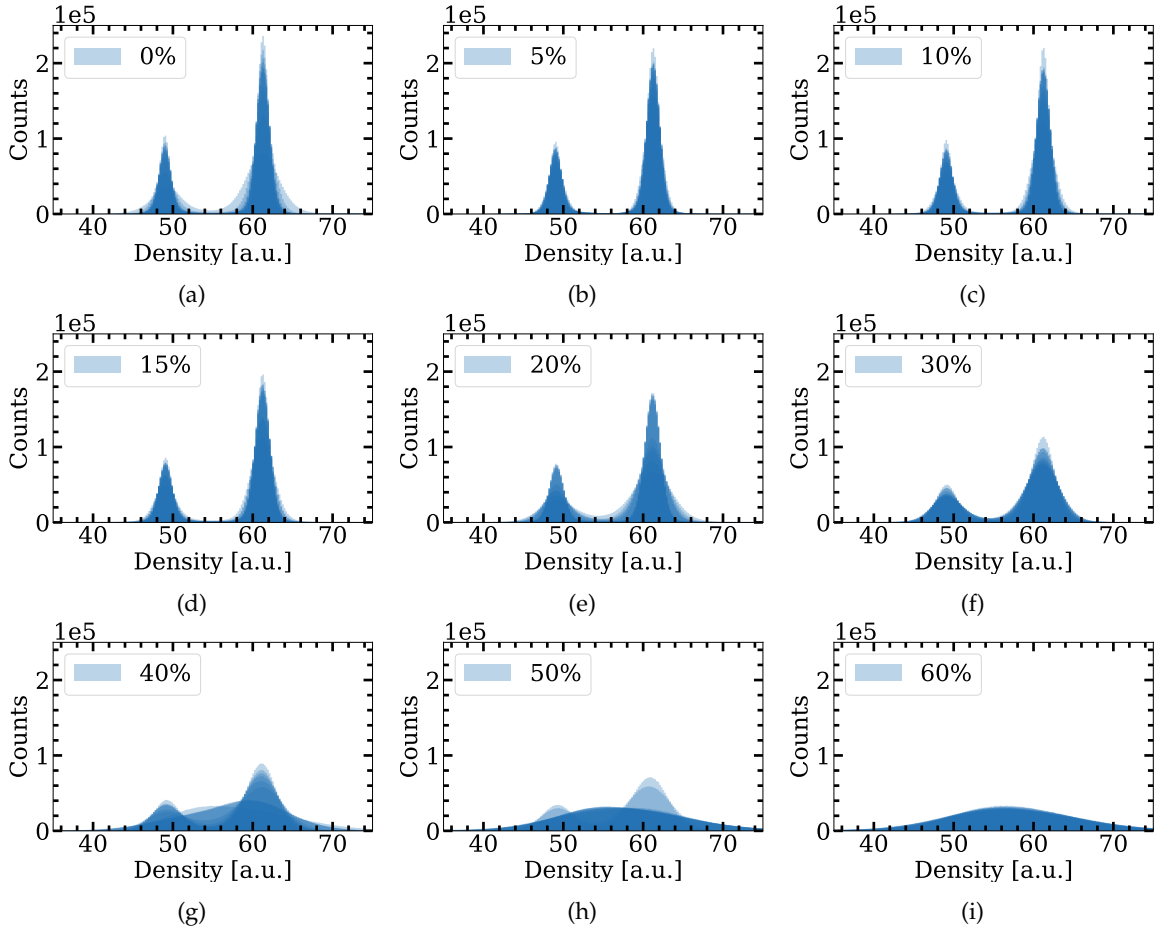

Figure 17: The density distributions for all the intensity reduction parameters examined in [49]. The intensity reduction is shown within the legend, as to indicate the colour of one single density distribution. For each parameter, the density distribution for the ten reconstructions are shown. As evident in the figure, the distributions became gradually wider with increasing intensity reductions. For the highest reductions, the two initial distributions were no longer separable for some of the reconstructions. Each distribution has the same colour, meaning that the darker colours stem from overlapping distributions.

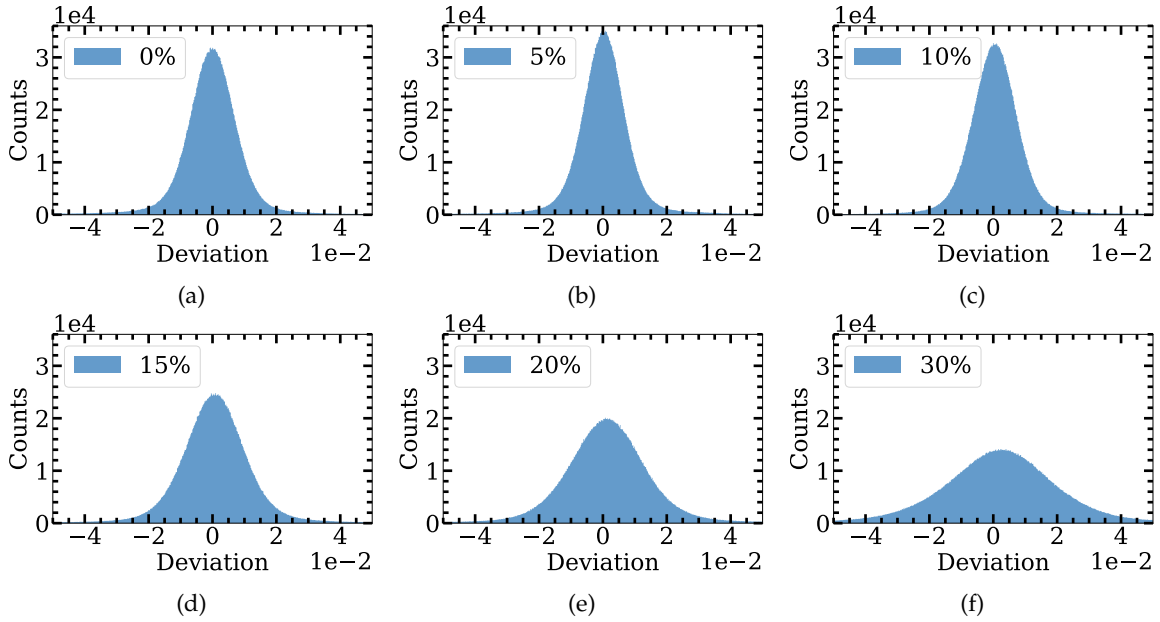

Figure 18: The deviation between the average of the normalised reconstructed objects and the initial object. The deviations were seen to increase with an increasing amount of Bragg scattering. As evident in Figure 31a, one of the reconstructions was significantly worse than the rest for the 0% reduction parameter, explaining the increase in deviation when going from (a) to (b). The reconstructions were normalised by fitting a Gaussian function to the rightmost peaks in Figure 17 and dividing the reconstruction with their respective mean value. Collected from [49].

4 METHOD

4.1 INTRODUCTION

The aim of this thesis was to further study the effects of Bragg scattering on CDI experiments, building on the work described in Section 3.5. In the previous work, it was found that Bragg scattering can have a significant negative impact on the phase retrieval process, given that the intensity of the forward diffracted beam was reduced sufficiently due to the Bragg scattering. Having seen this potential reduction in reconstruction quality, it was important to find a realistic estimate of how strong the intensity reduction due to Bragg scattering might be, how the intensity reductions varied as a function of the angular deviation from the Bragg condition, and eventually how this new information affected the phase retrieval process. Consequently, the work performed in this thesis was divided into two parts. The first part examined how much of the incoming beam was scattered of a simulated aragonite crystallite at different orientations close to the Bragg condition by performing a rocking curve analysis. The pattern found from these calculations was then utilised in the second part to see how it affected the CDI simulations described in Section 3.5.

4.2 SCATTERING CALCULATIONS

The goal of the scattering calculations was to find the relation between the intensity of the incoming and the scattered beam. This relation was then supposed to be used as a first approximation of how much intensity is lost in the forward direction when the crystal is oriented such that the Bragg condition is fulfilled or is close to being fulfilled. The intensity loss calculations were performed as a rocking curve analysis where the diffraction patterns of simulated, finite aragonite crystallites were computed for each orientation of the samples. The diffraction patterns were calculated using Equation (22) for a range of $\mathbf{Q}$-values close to the respective Bragg peak given by $\mathbf{G}_{hkl}$. More details on the samples, the detector system and the rocking curve analysis follow in the upcoming sections.

4.2.1 *Sample*

As mentioned, the samples were simulated single crystallites of aragonite, a polymorph of $CaCO_3$. The unit cell of aragonite is orthorhombic, with the lattice constants $a = 0.498$ nm, $b = 0.767$ nm and $c = 0.503$ nm [1]. One unit cell consists of four formula units, and the positions of the ions are known [1]. For the carbonate ions, it was assumed for simplicity that the oxygen atom lying closest to the carbon atom in the aragonite structure had a formal charge of 0, while the two others, positioned slightly further from the carbon atom, had a formal charge of -1.

Three different crystallite shapes were examined, namely a cuboid, an ellipsoid and a hexagonal prism which was elongated along the c-direction to mimic the pseudo-hexagonal crystal structure, as described by Bragg [9].

Additionally, three different sizes for each shape were examined. One was chosen such that the number of unit cells along each axis of the cuboid was equal to 600. This number was chosen because an aragonite sample studied with CDI by another member of the re-

search group had crystallite sizes around 300 nm[1], which roughly corresponds to 600 unit cells along each axis.

To have a similar volume, i.e. approximately equally many unit cells, for the cuboid, N_c, and the ellipsoid, N_e, the number of unit cells along each axis of the ellipsoid was set to 744. This follows from the relation between the volume of a cuboid and an ellipsoid,

$$\frac{V_c}{V_{uc}} = N_c = M_c^3 \approx \frac{4\pi}{3}\left(\frac{M_e}{2}\right)^3 = N_e = \frac{V_e}{V_{uc}}$$
$$\implies M_e \approx \left(\frac{6}{\pi}\right)^{\frac{1}{3}} M_c,$$

where M_c and M_e are the number of unit cells along each axis of the cuboid and ellipsoid, respectively, V_c and V_e are their respective volumes and $V_{uc} = abc$ is the volume of one unit cell. For $M_c = 600$, $(N_c - N_e)/N_c = 0.34\%$.

Similarly, the hexagonal prism had $600 \cdot 1.5 = 900$ unit cells along the c-axis, and 608 along the diagonal of the hexagon in the ab-plane. This time the number along the c-axis, $M_{h,c}$, was chosen such that the sample became approximately two times longer along the c-axis compared to the two other axes, and the number along the diagonal, $M_{h,diag}$ was chosen such that the number of unit cells in the hexagonal prism, N_h, was as equal to N_c as possible.

$$\frac{V_c}{V_{uc}} = N_c = M_c^3 \approx \frac{3\sqrt{3}}{8} M_{h,diag}^2 M_{h,c} \approx N_h = \frac{V_h}{V_{uc}},$$
$$M_{h,c} = \frac{3}{2} M_c,$$
$$\implies M_{h,diag} \approx \sqrt{\frac{16}{9\sqrt{3}}} M_c,$$

This time $(N_c - N_h)/N_c = -0.86\%$ for $M_c = 600$.

Besides the base size of 600 unit cells, crystallites having base sizes of 150 and 300 unit cells were also considered to examine the effect of crystallite size. For each of the base sizes, M_e, $M_{h,c}$ and $M_{h,diag}$ were found using the equations above.

In the following chapters, the different crystallites will be referred to using the following notation: $Shape_{size}$. The shape will be denoted by either C, E or H for the cuboid, ellipsoid and hexagonal prism, respectively, while the size will be given by the base size. To summarise, an ellipsoid crystallite having a base size of 300 will be referred to as E_{300}.

4.2.2 *Calculating the diffraction pattern*

To calculate the diffraction pattern, the differential scattering cross section had to be calculated. This was done using the kinematical approximation, more specifically Equation (22). The calculations of the scattering amplitudes were performed using the python package PyNX, mentioned in Section 3.5. The atomic form factors were calculated using Cromer-Mann coefficients and a set of dispersion correction factors, as described in Section 2.2.2.1 and 2.2.2.2, respectively. The values of the Cromer-Mann coefficients and the dispersion corrections used in this thesis are listed in Table 1 and 2 and were collected from [14] and [46], respectively. The dispersion corrections were chosen based on the energy of the incoming radiation, which in these simulations was 8.051 keV. This X-ray energy was chosen because it is in the range of energies typically used in CDI experiments.

To find the total diffracted intensity for each orientation of the crystallite, an integration over $\mathbf{Q}$ close to $\mathbf{G}_{hkl}$ had to be performed, as described in the next section.

1 D. Younas et al., to be published

Table 1: The Cromer-Mann coefficients used to calculate the atomic form factors. Note that only four decimals have been included in the table. See [14] for the complete list.

Cromer-Mann coef.	Ca^{2+}	C	O	O^{-}
a_1	15.6348	2.2607	3.4850	4.1160
a_2	7.9518	1.5617	2.2680	1.6369
a_3	8.4372	1.0508	1.5463	1.5267
a_4	0.8537	0.8393	0.8670	−20.3070
b_1	−0.0074	22.6907	13.2771	12.8573
b_2	0.6089	0.6567	5.7011	4.1724
b_3	10.3116	9.7562	0.3239	47.0179
b_4	25.9905	55.5949	32.9089	−0.0140
c	−14.8750	0.2870	0.2508	21.9412

Table 2: The dispersion corrections used in the simulations. The values were found in [46].

Dispersion correction	Ca	C	O
$\Delta f'$	0.3402	0.0168	0.0464
$\Delta f''$	1.2847	0.0090	0.0322

4.2.3 *Detector*

Due to the finite size of the crystal, a range of scattering vectors **Q** will give a significant signal, as explained in Section 2.2.5. A two-dimensional detector was therefore simulated to collect the scattered intensity. The detector was set to be flat with its normal vector pointing in the direction of the scattered wave vector fulfilling the Bragg condition. It had 200 pixels in each direction, hereby known as D_x and D_y. The size of the pixels was different when examining crystallites of different sizes. When the base size of the objects, M, was 150, every pixel was 10 µm × 10 µm. For the two other base sizes, the pixel size was decided by multiplying 10 µm with 150/M. This scaling was done to save computational time while still being able to resolve the finer features of the diffraction pattern. Because of the relation between sizes in real and reciprocal space, as described in Section 2.2.5, the scattered intensity from the larger crystallites will be spread out over a smaller region in reciprocal space, corresponding to a smaller detector.

The detector was assumed to be ideal, i.e. no read-out noise or dark pixels etc. It should also be noted that the pixel size was smaller than today's state-of-the-art detectors, such as the Medipix-3 developed at CERN, which has a pixel size of 55 µm × 55 µm [3]. However, this was of no importance for the simulations since the intensity scattered from the sample was constant across a solid angle. Therefore, the detector could have had a pixel size similar to real detectors, and simply be placed further away from the sample to retrieve the same signal. Also, the intensity measured with real detectors could easily be decided by averaging over multiple of the simulated pixels. In the simulations performed in this thesis, the detector was placed 5 cm from the sample.

Since the calculations were performed numerically, the detector was a set of discrete, equidistant points rather than a true two-dimensional object, as illustrated in Figure 19. One scattering vector was calculated for each point, taking the curvature of the Ewald sphere into account. Instead of measuring the intensity at every pixel, as in a real experiment, the scattered flux, i.e. $\Phi = \Phi_0(d\sigma/d\Omega)/R^2$, was computed for each scattering vector. By

assuming that the flux was constant over each pixel, the intensity, I_{pixel}, could be found by multiplying the flux with the area, ΔA, which the detector was supposed to cover, as described in Equation (32).

$$I_{pixel} = \Phi \Delta A = \Phi_0 \frac{d\sigma}{d\Omega} \frac{\Delta A}{R^2} \approx \Phi_0 \frac{d\sigma}{d\Omega} \frac{R^2 \Delta \Omega}{R^2} \approx \Phi_0 \frac{d\sigma}{d\Omega} \frac{\delta x \delta y}{R^2},$$

where δx and δy are the sidelengths of the assumed pixel and R is the distance from the sample to the detector. The solid angle was assumed to be equal $\delta x \delta y / R^2$ for all points. This approximation is valid due to the large distance between the sample and the detector compared to the size of the detector as well as the orientation of the detector compared to the scattered beam, see Figure 20. The assumption that the intensity is equally distributed over an entire pixel is not true for a real detector. However, it is likely that the random variation of the calculated intensity versus the real intensity would not have a significant impact on the results. Finally, the scattered intensity for each rotation was found by summing over the pixel values, i.e. $I_{sc} = \sum I_{pixel}$.

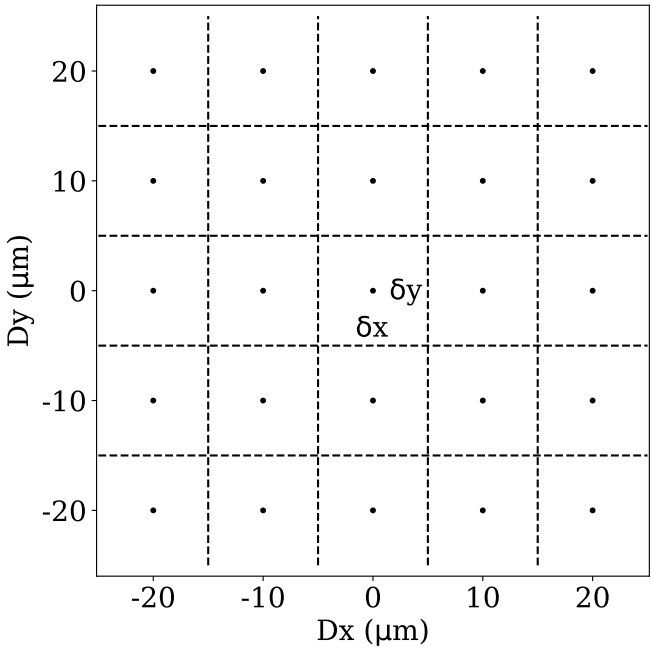

Figure 19: An illustration of a detector showing the 25 pixels closest to the centre of the detector. The flux calculated at each point was assumed to be representative for their respective pixel, given by the dotted lines. The size of the pixels corresponds to the detector that was used to study the smallest crystallites.

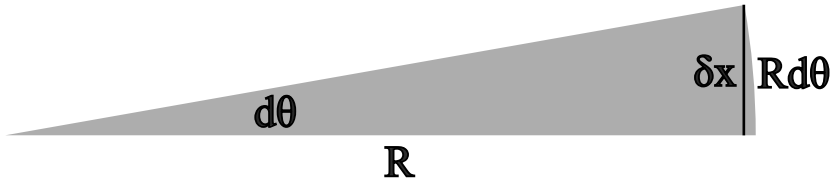

Figure 20: The relation between the side lengths of the detector pixels and the angle they cover. It is clear that for small angles, i.e. when $R >> \delta x$, $\delta x \approx R d\theta$, because $\sin(d\theta) \approx d\theta$. Since the detector is set to be normal to the scattered beam, one will have a similar expression for the angle covered by δy. Hence, the total solid angle covered by one detector pixel can be written as $\Delta\Omega \approx \delta x \delta y / R^2$

The coordinates of the scattering vectors at the detector are given in the hypothetical fixed experimental coordinate system, as shown in Figure 21 and 22. Following the discussion in Section 2.2.5, the real space lattice, A, and the reciprocal lattice, B, can be described by the following matrices

$$\begin{aligned} A &= \begin{bmatrix} \mathbf{a}_1 & \mathbf{a}_2 & \mathbf{a}_3 \end{bmatrix}, \\ B &= 2\pi A^{-1} = \begin{bmatrix} \mathbf{b}_1 & \mathbf{b}_2 & \mathbf{b}_3 \end{bmatrix}, \end{aligned} \tag{48}$$

where $\mathbf{a}_i$ are the real space lattice vectors and $\mathbf{b}_i$ are the reciprocal lattice vectors. For an orthorhombic lattice, the lattice vectors can be oriented along the experimental axes, i.e. the x-, y and z-axis in Figure 22. In the simulation performed in this thesis, the $\mathbf{a}_1$-, $\mathbf{a}_2$- and the $\mathbf{a}_3$-axis of the crystal were initially aligned with the x-, y- and the z-axis of the coordinate system, respectively, before the crystallites were rotated to fulfil the Bragg condition. To rotate the crystallites, the normal vector of the examined lattice planes was first aligned with the x-axis, before the crystallite was rotated θ_B around the y-axis. At the crystal's initial position, the lattice vectors were described by

$$\mathbf{a}_1 = \begin{bmatrix} a \\ 0 \\ 0 \end{bmatrix}, \ \mathbf{a_2} = \begin{bmatrix} 0 \\ b \\ 0 \end{bmatrix}, \ \mathbf{a}_3 = \begin{bmatrix} 0 \\ 0 \\ c \end{bmatrix}, \tag{49}$$

where the column vectors follow the standard notation with x being the first coordinate, then y and lastly z.

The reciprocal lattice vectors are defined by the following equation

$$\mathbf{G}_{hkl} = h\mathbf{b}_1 + k\mathbf{b}_2 + l\mathbf{b}_3 = \begin{bmatrix} \mathbf{b}_1 & \mathbf{b}_2 & \mathbf{b}_3 \end{bmatrix} \begin{bmatrix} h \\ k \\ l \end{bmatrix} = B \begin{bmatrix} h \\ k \\ l \end{bmatrix}. \tag{50}$$

When rotating the crystallite, described by the rotation matrix R, the reciprocal lattice is rotated equally. This can be seen from Figure 5 illustrating the relation between the reciprocal lattice vectors and the normal vectors of the lattice planes. Therefore, the value of the scattering vector at the centre of the detector have to be equal

$$\mathbf{Q} = R\mathbf{G}_{hkl} = RB \begin{bmatrix} h \\ k \\ l \end{bmatrix}. \tag{51}$$

From this, one can prove that the scattering vector values used in this experiment in fact correspond to the correct hkl-values.

$$\begin{bmatrix} h \\ k \\ l \end{bmatrix} = B^{-1}R^{-1}\mathbf{Q} = \frac{1}{2\pi} A R^{-1}\mathbf{Q} = \frac{1}{2\pi} A^T R^T \mathbf{Q} = \frac{1}{2\pi} (RA)^T \mathbf{Q} \tag{52}$$

$$\begin{aligned} 2\pi h &= x_a * Q_x + y_a * Q_y + z_a * Q_z, \\ \implies 2\pi k &= x_b * Q_x + y_b * Q_y + z_b * Q_z, \\ 2\pi l &= x_c * Q_x + y_c * Q_y + z_c * Q_z, \end{aligned}$$

where the relation $R^{-1} = R^T$ is valid for all rotation matrices and $A = A^T$ for an orthorhombic lattice. x_a corresponds to the distance travelled in the x-direction of the fixed coordinate

system when moving one unit cell along the $\mathbf{a}_1$-axis of the crystallite. Similarly, y_a is the distance in the y-direction when moving one unit cell along the $\mathbf{a}_1$-axis of the crystallite. The rest follow the same pattern. The relationship between the scattering vector values in the fixed coordinate system and the hkl-values of the rotated crystallite is shown in Figure 21 for the detector used to study the smallest crystallites.

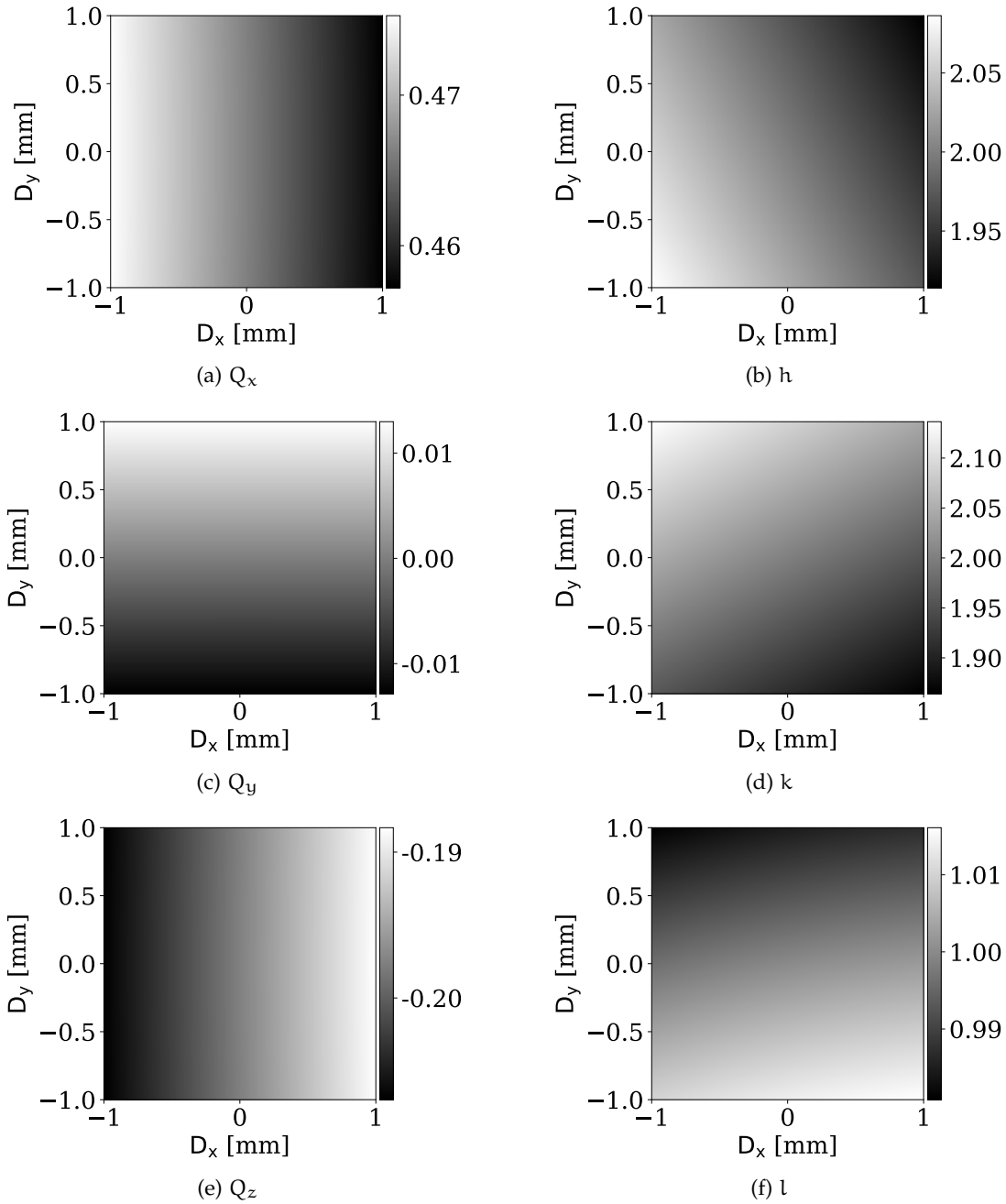

(a) Q_x (b) h

(c) Q_y (d) k

(e) Q_z (f) l

Figure 21: The values of the scattering vectors at each detector pixel when studying a sample with a base size of 300 are shown in (a), (c) and (e). Their corresponding hkl-values when studying the (221) reflection are shown in (b), (d) and (f). As expected, $Q_y \approx 0$ since the detector was placed in the xz-plane. The hkl-values are distributed around the correct values given by the reflection.

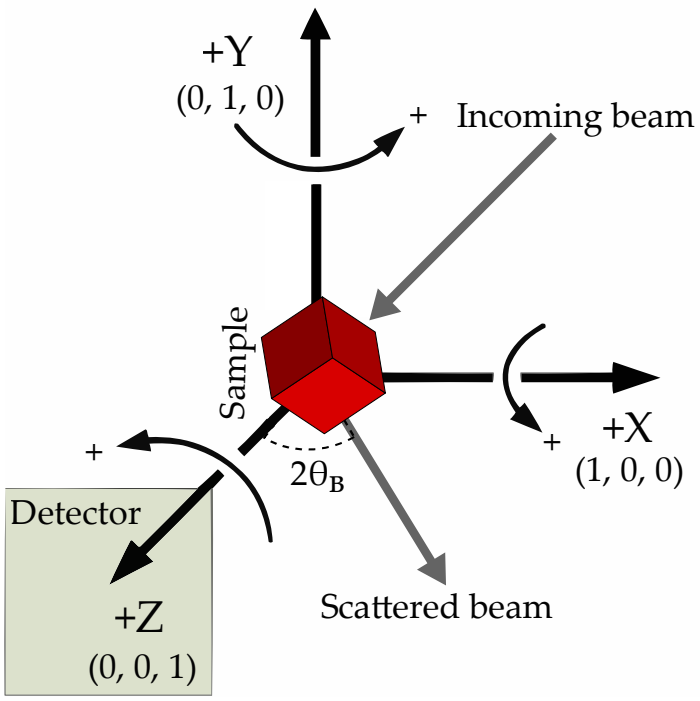

Figure 22: The experimental setup. The detector was placed 5 cm from the sample. For each reflection, the detector had to be rotated $2\theta_B$ around the y-axis from its initial position in the forward direction to measure the scattered beam. Adapted from the NeXus manual[2].

4.2.4 *Calculating the relation between the scattered and incoming flux*

The relation between the scattered and incoming flux has been calculated for two situations. Firstly, the maximum scattered flux, $(\Phi_{sc})_{max}$, was calculated for the reflections in Table 3. Then, the scattered flux for two orientations of the samples was calculated for the entire detector.

The calculations of $(\Phi_{sc})_{max}/\Phi_0$ differ from the rest of the calculations. Here, only cuboid samples were examined. They had base sizes ranging from 10 to 800. Additionally, the samples were not rotated, as the maximal scattered flux will only be measured when the sample fulfils the Bragg condition. The detector was also different. It only consisted of one pixel, i.e. the centre pixel, as the maximal value of the scattered flux necessarily will be measured when $\mathbf{Q} = \mathbf{G}_{hkl}$, which should be the case in the centre of the detector. These calculations were mainly performed to validate that the calculated values were consistent with the theoretical values expected from Equation(31).

When calculating the flux across the entire detector, the detectors that were described in Section 4.2.3 were used. As mentioned, two orientations of the samples were studied, namely the orientation that fulfilled the Bragg condition and a orientation where the samples had been rotated 0.2° around the y-axis compared to the Bragg condition. The (221) reflection of two ellipsoidal samples, namely E_{600} and E_{150}, were analysed

4.2.5 *Rocking curve analyses*

After looking at how the scattered flux was distributed across the detector for two different orientations of the examined samples, the scattered intensity was calculated for a range of orientations around the Bragg condition. A rocking curve analysis was performed for each

2 The manual can be found at https://manual.nexusformat.org/. The figure was collected on the 17th of June 2023.

Table 3: The scattering planes used in the calculations and their corresponding Bragg angles with one decimal accuracy. The relative intensity is calculated based on the unit cell structure factor at the Laue condition. The values were calculated for an incoming beam having an energy of 8.051 keV.

Reflection (hkl)	$2\theta_B$	Relative intensity
(400)	76.9	100
(221)	45.9	82
(111)	26.2	31
(100)	18.9	0

reflection listed in Table 3, for each of the samples mentioned in Section 4.2.1. The scan sampled one diffraction pattern every 1 m° from $-0.1°$ to $0.1°$ around the Bragg condition. The diffraction pattern was calculated as explained in Section 4.2.2 and the samples were rotated around the y-axis shown in Figure 22. For all the calculations, the incoming beam was taken to be a perfect, non-divergent plane wave with an energy of 8.051 keV, as mentioned previously.

The goal of the calculations was to find the relation between the scattered intensity and the incoming intensity for each orientation of the sample, i.e. I_{sc}/I_0, starting from Equation (32), which is repeated and elaborated on here for simplicity

$$I_{sc} = \Phi_0 \int_{Det} \frac{d\sigma}{d\Omega} d\Omega = \sum_{Det} I_{pixel} = \Phi_0 \sum_{Det} \frac{d\sigma}{d\Omega} \frac{\delta x \delta y}{R^2}.$$

From here it was assumed that the incoming intensity, I_0, could be found by multiplying the incoming flux with the area of the sample. In other words

$$\begin{aligned} I_{sc} &= \Phi_0 \frac{A_{sample}}{A_{sample}} \sum_{Det} \frac{d\sigma}{d\Omega} \frac{\delta x \delta y}{R^2} \\ \implies \frac{I_{sc}}{I_0} &= \frac{1}{A_{sample}} \sum_{Det} \frac{d\sigma}{d\Omega} \frac{\delta x \delta y}{R^2}. \end{aligned}$$

This is however a simplification which cannot be correct as it does not take the depth of the sample into account. All the values of I_{sc}/I_0 must therefore be seen as initial estimates. Since this procedure already is a simplification of the true picture, the area of the sample was assumed to be $Ma \cdot Mb$ for all the samples, where M is the base size and a and b are the lattice parameters of the aragonite crystallite.

4.3 SIMULATING THE EFFECTS OF BRAGG SCATTERING IN A CDI EXPERIMENT

In the second part of this thesis, the effects of Bragg scattering on a simulated CDI experiment have been analysed. This was done by creating an initial object digitally, before calculating the diffraction pattern of this object and reducing the intensity for some of the projections. Finally, the object was reconstructed again and the deviations from the initial object were studied. The details of this will be explained in the following sections.

The procedure described below is the same as the one found in [49], i.e. the project work performed by the author the past autumn, except for the intensity reduction filters that were applied to the diffraction pattern to simulate the Bragg scattering. These filters are described more thoroughly in Section 4.3.2.2. By slightly altering the procedure, it was

possible to see the effects of the updated information on the Bragg scattering, which was obtained from the scattering calculation outlined in Section 4.2.

4.3.1 *Object generation*

The examined object consisted of two overlapping ellipsoids. It was constructed digitally using Python. The two ellipsoids had different sizes and densities, where the orange ellipsoid in Figure 23, i.e. the lower one in Figure 23a, had a relative density of 1, and the green ellipsoid had a relative density of 0.8. The ellipsoids were created within a matrix of $256 \times 256 \times 256$ voxels. The details of the structure can be found in Table 4, and three overview images can be seen in Figure 23.

There were multiple reasons for choosing two overlapping ellipsoids. Firstly, ellipsoids are simple objects that are easy to construct digitally. Secondly, by altering the length of the semi-axes, one can create other common structures, such as disks, rods and spheres. Thirdly, the diffraction pattern of ellipsoids contains fewer high-frequency components than other simple objects, such as cubes. This means that more of the information is kept in the low-frequency components, which is what one measures in CDI. Of course, an object constructed digitally will consist of many small cubes, each giving rise to a high-frequency component in the diffraction pattern, but the overall morphology is better kept for an ellipsoid than for a cube. Lastly, by examining two objects of different densities, one could see how well the density distribution was preserved in the reconstructions.

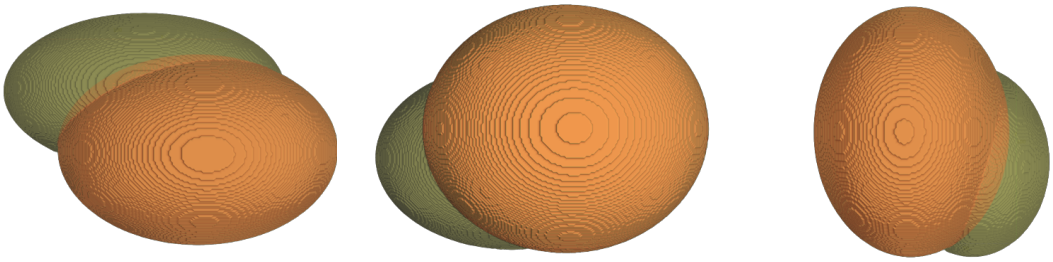

(a) The initial object viewed from the front.

(b) The initial object viewed from the bottom.

(c) The initial object rotated and viewed from the right.

Figure 23: The initial object viewed from three different directions. The orange area has a relative density of 1, while the green has a relative density of 0.8. The object is the same as in [49], as depicted in Figure 15.

Table 4: Details of the examined object. Centre is defined in relative coordinates compared to the system size of $256 \times 256 \times 256$ voxels. The sizes of the ellipsoids are given as tuples containing the semi-axes for the ellipsoids, in the x, y and z direction, respectively. These are also given relative to the system size. For the overlapping parts, the ellipsoid with the lowest density was removed.

Description	**Rel. density**	**Size**	**Centre**
Orange	1.0	(0.25,0.32,0.37)	(0.57,0.51,0.61)
Green	0.8	(0.22,0.27,0.40)	(0.41,0.43,0.47)

4.3.2 *Diffraction*

To simulate the diffraction process, the python package PyNX, mentioned in Section 3.5, was used. Perfect conditions were assumed under the diffraction simulation, i.e. a perfectly coherent beam, no beam stop or other imperfections of the experimental setup. This was done to focus on the effect of the intensity reductions. In other words, removing factors that might affect the reconstruction process, thereby making it more difficult to compare the results.

4.3.2.1 *Ensuring sufficient oversampling*

To ensure a sufficient degree of oversampling, as described in Section 3.3, the diffraction pattern was sampled with twice as many voxels in each dimension as compared to the initial $256 \times 256 \times 256$ grid, i.e. $512 \times 512 \times 512$ voxels. This means sampling with a frequency of $1/(2 \times \mathtt{system\ size})$, where the system size is the size of the initial grid in voxels. This degree of oversampling was significantly higher than required, since the diffraction pattern was sampled at a factor which is larger than two times the size of the object in every direction.

4.3.2.2 *Simulating the diffraction pattern - Applying Bragg scattering*

To calculate the diffraction pattern, the scattering amplitude of each part of the object was calculated, so that they later could be added together and squared to get the diffraction intensity, as shown in Equation (36). Before this, the scattering amplitude of certain projections for certain parts of the objects was reduced. By applying this reduction to only certain parts of the sample, one could simulate the situation of having a partly crystalline sample, or a sample where the crystalline parts were oriented in different directions. Here, as in [49], the sample was assumed to consist of two single crystalline domains, i.e. one domain per ellipsoid. Additionally, it was assumed that they only fulfilled the Bragg condition once, and that they fulfilled it at an angle of 20° compared to each other. The reduction itself was done by applying a two-dimensional filter to the three-dimensional scattering amplitude matrix. This was done along the z-axis of the array, so that the z-axis of the simulations corresponds to the z-axis of a real experiment, as shown in Figure 22. An example of an applied filter can be seen in Figure 24. Here, an intensity reduction of up to 10% has been applied. The reduction decreases from the maximum to zero following a normal distribution.

The reduction is a reduction in intensity. This means that if it is said that an intensity reduction of 10% has been applied, it is really a $\sqrt{10}$% that has been applied to the scattering amplitude, which later has been squared to get the intensity, and thus having an intensity reduction of 10%. In total, 9 different intensity reductions were applied, namely 0%, 5%, 10%, 15%, 20%, 30%, 40 %, 50% and 60%, all having the same shape of the reduction filter as the one shown in Figure 24.

After having reduced the scattering amplitude for some of the projections, they were added together and squared to get the overall intensity. The intensity was then normalised to 10^{10} photons to improve the reproducibility of the reconstruction process and to better be able to compare the effect of the different reductions, as the density of the reconstructed objects scaled with the intensity of the diffraction pattern.

4.3.3 *Reconstructing the objects*

To reconstruct the objects from the diffraction patterns, the same Python package as mentioned in Section 4.3.2, PyNX, was used. To initialise the reconstruction, a suitable support had to be decided. This was chosen to be a sphere with a radius that was known to be

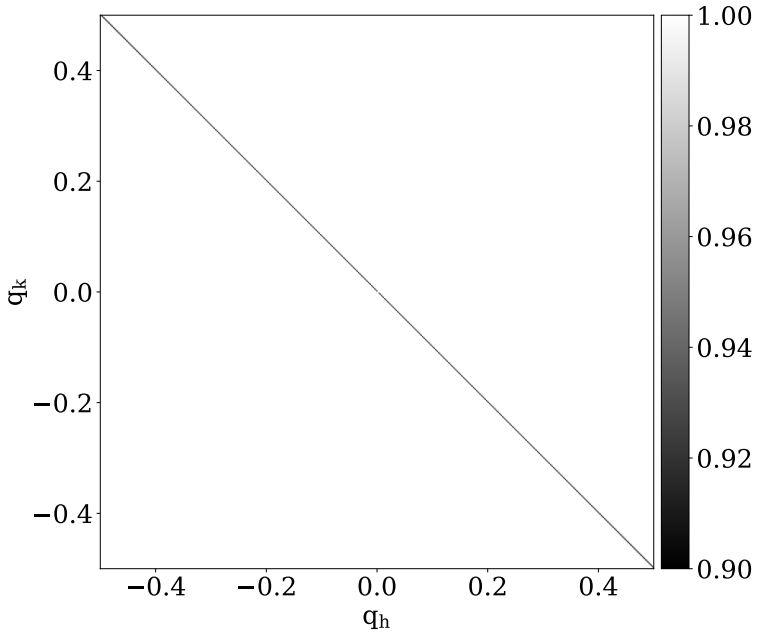

Figure 24: Illustration of a filter that was applied to the diffraction pattern to simulate the reduction in intensity due to Bragg scattering. Here, a 10% reduction would have been applied. Note that this filter is considerably narrower than the ones used in [49], as shown in Figure 16.

larger than the sample by looking at the autocorrelation function as described in Section 3.3. The support was later periodically updated using a function of the software, similar to the algorithm described in Section 3.4.3.

The phase of the objects were retrieved using a combination of the different algorithms described in Section 3.4. More precisely, 150 iterations of the HIO algorithm, with a support update every 25th iteration, were applied, before 24 iterations of the detwinning HIO algorithm were used. Then 400 iterations of the HIO algorithm with a support update every 25th iteration were performed. Finally, 400 iterations of the ER algorithm, again with a support update every 25th iteration, were applied. This algorithm was chosen because it provided reasonable reconstructions within reasonable time limits. A further study comparing different reconstruction algorithms was not performed.

To have representative reconstruction data, 10 reconstructions were done for each intensity reduction parameter. In contrast to a real experiment, where one typically chooses a collection of the best reconstructions, all the reconstructions were kept for the following error analysis. This was done to see the entire impact of the intensity reductions on the reconstruction quality, so as to not hide the most inaccurate results.

4.3.4 *Error analysis*

To analyse the reconstruction quality, multiple quantities were examined. This was done with multiple Python scripts, which can be found at `https://github.com/SigurdStene/TFY4905_spring23/CDI`.

The first quantity that was examined was the density distribution of the reconstructed objects. This was done by fitting two Gaussian functions to the density data and comparing the mean, μ, and standard deviation, σ, of the two distributions. These values will be referred to as μ_h, σ_h, μ_l, and σ_l, where the subscript h and l refer to the high and low-density regions, respectively. Additionally, an extra subscript might sometimes be used, for example, $\mu_{h_{10}}$, to indicate which intensity reduction parameter was used, here exemplified by a reduction of 10%. In order to fit these Gaussian functions, the density data was first

binned into 500 bins. The same bins were used for all the reconstructions. All the values were calculated based on the 10 reconstructions for each intensity reduction parameter, i.e. by first calculating the value of μ_h, σ_h, μ_l, and σ_l for each reconstruction and then finding the final value by looking at the mean of these values. The uncertainties are given by the standard deviation from this process.

The ratio between the two means, $r_\mu = \mu_l/\mu_h$, was calculated to see how well the densities of the initial object had been kept in the reconstructions. This was then compared to the ratio of the initial object of 0.8, as given in Table 4. Additionally, the ratio between the areas under the two functions, r_a, was calculated. To calculate r_a, the areas under the two Gaussian functions were compared. These were found from the known integral of a Gaussian function, which is given by:

$$\int_{-\infty}^{\infty} a e^{-\frac{(x-\mu)^2}{2\sigma^2}} dx = a\sqrt{2\pi\sigma^2}, \tag{53}$$

where a is the maximum value of the distribution. Hence, one can look at the ratio between the areas as:

$$r_a = \frac{\int_{-\infty}^{\infty} a_h e^{-\frac{(x-\mu_h)^2}{2\sigma_h^2}} dx}{\int_{-\infty}^{\infty} a_l e^{-\frac{(x-\mu_l)^2}{2\sigma_l^2}} dx} = \frac{a_h\sqrt{2\pi\sigma_h^2}}{a_l\sqrt{2\pi\sigma_l^2}} = \frac{a_h\sigma_h}{a_l\sigma_l}. \tag{54}$$

An example of two fitted functions is shown in Figure 25.

To minimise the effect of random fluctuations in the density distribution, the average reconstructed objects were also analysed. To calculate these, all the reconstructions per intensity reduction parameter were aligned as best as possible, before their average was calculated. The average objects, as they will be referred to from now, were then analysed in a similar same way as the individual reconstructions.

The second quantity that was examined was the deviation from the initial structure. To do this, the average objects were normalised. This was done by dividing them by their respective μ_h value. The deviation from the initial structure was analysed by aligning the mean reconstructed objects with the initial object and subtracting them from each other.

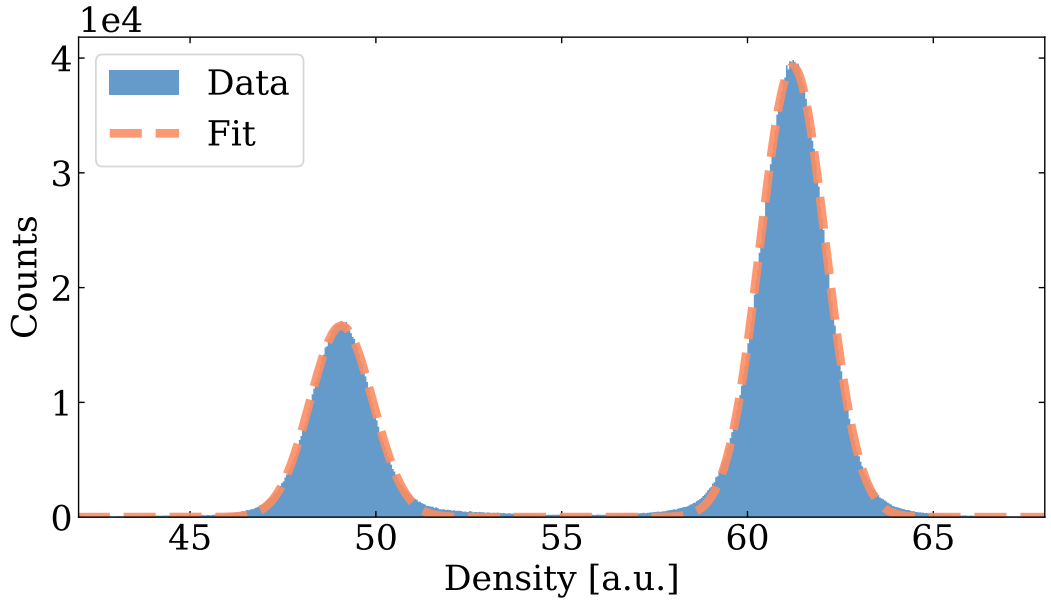

Figure 25: Example of two Gaussian functions which have been fitted to the density distribution of a reconstructed sample.

5 RESULTS AND DISCUSSION

5.1 OVERVIEW

The scattering calculations performed on the finite, simulated aragonite crystallites indicated that the incoming beam will not lose any intensity except from a narrow region around the Bragg condition. For the largest crystallites, i.e. the crystallites having a base size of 600 unit cells, corresponding to a diameter of 300 nm to 500 nm, this range was less than $\pm 0.1^\circ$. By applying the intensity reductions over this range, the phase retrieval process was found to improve significantly compared to the results found in the project work performed by the author [49]. An increased deviation from the initial object with an increasing intensity reduction was observed. However, these deviations were small compared to the deviations in [49], and all the reconstructed objects were qualitatively the same as the initial object. A more thorough description of the results is given in the following sections.

5.2 SCATTERING CALCULATIONS

5.2.1 *The maximum flux of the scattered radiation*

The ratio between the maximum flux of the scattered beam, $(\Phi_{sc})_{max}$, and the flux of the incoming beam, Φ_0, has been analysed for cuboid samples with a range of crystallite sizes, N, for four different reflections, i.e. (400), (221), (111) and (100), as explained in Section 4.2.2. The results for the (400), (221) and (111) reflections are presented in Figure 26. Figure 26a shows how the value of $(\Phi_{sc})_{max}/\Phi_0$ ranged from a minimum value of 1.8×10^{-17}, 1.5×10^{-17} and 5.9×10^{-18} to a maximum value of 5.0×10^{-6}, 4.1×10^{-6} and 1.6×10^{-6} for the (400), (221) and (111) reflections, respectively. The figure also demonstrates how the maximum flux increases approximately as a function of N^2, as expected from Equation (31). Similarly, Figure 26b proves that the relative deviation between the calculated and the theoretical values was less than 4%, which was deemed sufficiently accurate for the purpose of the scattering calculations performed in this thesis. The (100) reflection has been excluded from Figure 26 since it is a forbidden reflection, thus having a significantly lower flux.

The development of $(\Phi_{sc})_{max}/\Phi_0$ has been fitted against the number of unit cells as

$$\log_{10}((\Phi_{sc})_{max}/\Phi_0) = a \log_{10}(N) + b,$$

such that

$$(\Phi_{sc})_{max}/\Phi_0 = 10^{a \log_{10}(N)+b} = N^a 10^b.$$

From Equation (31) it is expected that $a \approx 2$, and that $b \approx \log_{10}(|F^{uc}|^2 r_0^2/R^2) = b_{th}$. The results from the curve fitting are given in Table 5. The parameters for the (100) reflection have been included to show how they did not follow the same pattern as the rest. Additionally, b_{th} has been included to see how well the curve-fitting parameters agreed with the theoretical values.

From Figure 26 and Table 5 it is evident that the simulations were able to replicate the theoretically expected values to a sufficient degree. However, one cannot draw many conclusions from these results, as the scattered flux is only calculated at an infinitesimal point,

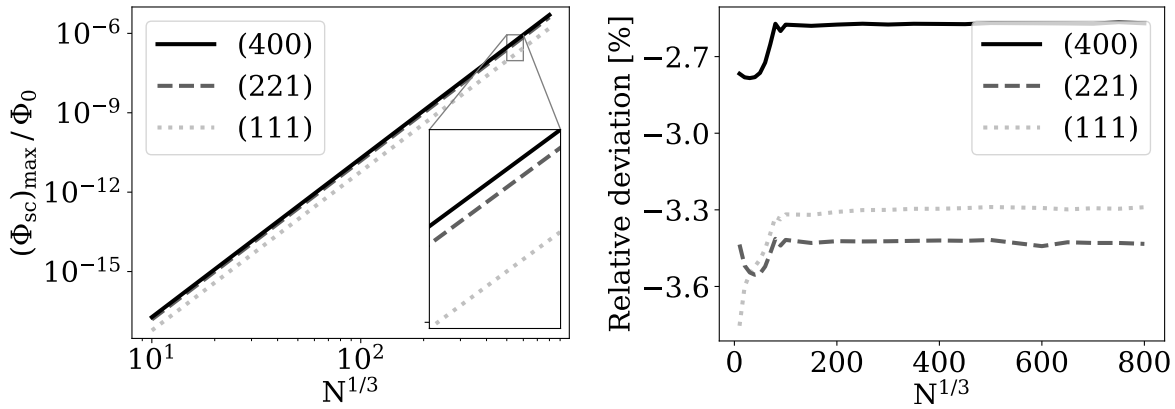

(a) (b)

Figure 26: The relation between the maximum scattered flux and the incoming flux. (a) highlights how the scattered flux increases as a function of the number of unit cells squared, as expected. (b) shows the deviation between the theoretical value and the calculated value.

Table 5: Curve-fit parameters. The values were in good agreement with the theoretical values for the (400), (221) and (111) reflections.

Reflection (hkl)	a	b	b_{th}
(400)	2.000	−22.72	−22.71
(221)	2.000	−22.81	−22.80
(111)	2.000	−23.23	−23.20
(100)	1.333	−24.49	-∞

and thus not directly relatable to the scattered intensity, which will vary across the detector. These variations will be studied in Section 5.2.2.

Additionally, since the kinematical approximation will break down when increasing the crystallite size, one cannot extrapolate the lines in Figure 26a using the parameters in Table 5 without a further investigation of whether dynamical effects must be taken into account.

Above, it was claimed that the calculated values of $(\Phi_{sc})_{max}/\Phi_0$ were similar to the theoretical values to a sufficient degree. However, they were not equal. When the crystallites were rotated to fulfil the Bragg condition, the necessary rotation angles were calculated based on the lattice parameters. They only had four decimals. Therefore, small errors were bound to arise when the matrices with the atoms' position were rotated based on these values. The h, k and l values at the detector have been calculated using the approach outlined in Section 4.2.3. Deviations up to 0.0007 from the expected values were found. All the calculated hkl-values for the examined reflections are listed in Table 6. These discrepancies are likely the cause of deviations seen in Figure 26b.

Table 6: The examined reflections and the hkl-values the detector's centre pixel appeared to have for the crystallites when they had been rotated to fulfil the Bragg condition.

Reflection (hkl)	h_{det}	k_{det}	l_{det}
(400)	4.0003	0.0005	−0.0002
(221)	2.0001	2.0007	0.9999
(111)	1.0002	1.0007	1.0001
(100)	1.0003	0.0005	−0.0001

5.2.2 *The scattered flux away from the Laue condition*

The previous section demonstrated that $(\Phi_{sc})_{max}$ scaled as N^2. Away from the Laue condition, the incoming flux is expected to decrease rapidly. This reduction is studied in Figure 27 and 28 for the (221) reflection of E_{600} and E_{150}[1], respectively. In Figure 27a, 28a, 27c and 28c the flux has been plotted for two different orientations of the crystallites. The two former present the flux when the crystallites fulfilled the Bragg condition, while the crystallites had been rotated 0.2° away from the Bragg condition around the y-axis in the two latter. For the rotated crystallites, the flux was generally weaker. At the centre of the diffraction spot, the flux was reduced with more than four orders of magnitude for E_{600}, while the flux was reduced with approximately two orders of magnitude for E_{150}. Both reductions prove that the amount of scattered intensity is highly dependent on the orientation of the crystallite.

Two lines have been drawn in each of the aforementioned figures to further study the local variations of the scattered flux. Variations of several orders of magnitude were seen along the lines. The dashed lines cross the centre of the detectors, while the dotted lines are 10 pixels below, i.e. 25 µm and 100 µm for E_{600} and E_{150}, respectively. 25 µm is less than the size of real detector pixels. Hence, a real detector could not detect the local differences presented in Figure 27 and 28. The trend would, however, be the same, with a sharp decrease from the centre of the detector, and a reduction when rotating the crystal away from the Bragg condition.

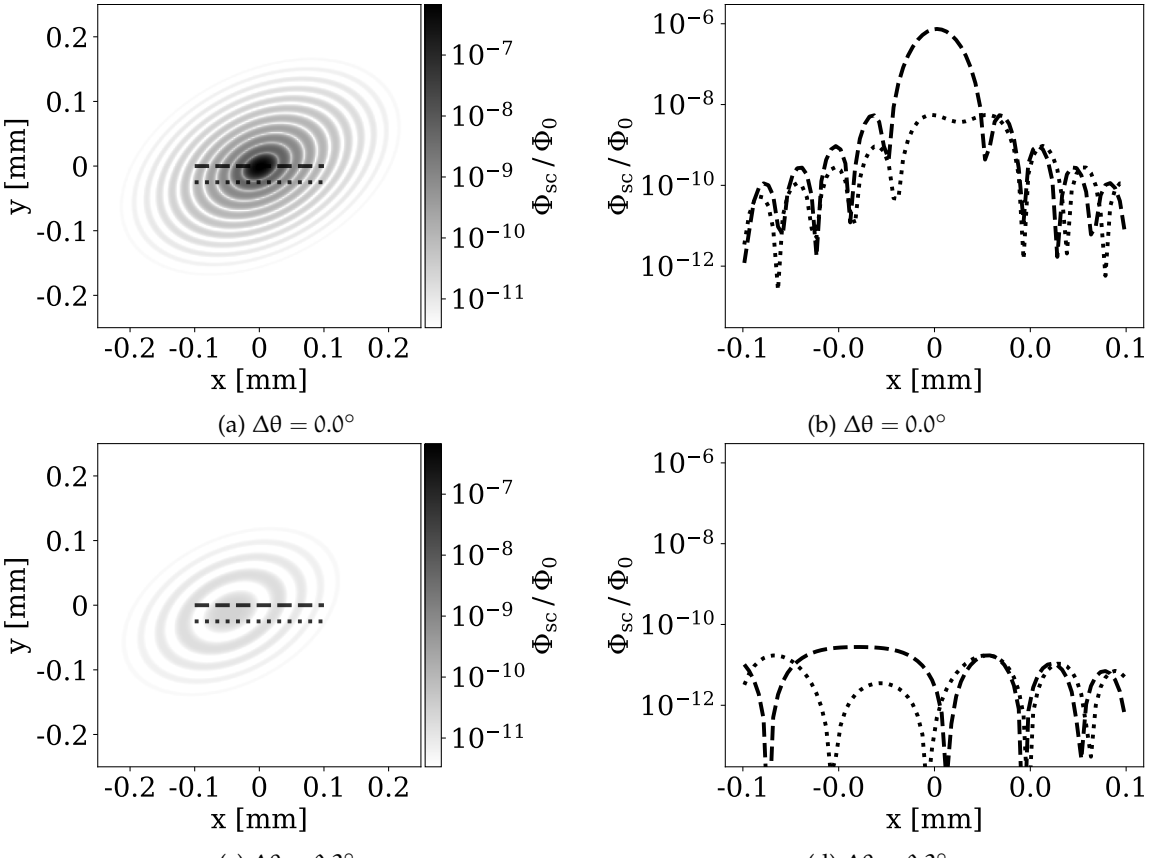

(a) $\Delta\theta = 0.0°$ (b) $\Delta\theta = 0.0°$

(c) $\Delta\theta = 0.2°$ (d) $\Delta\theta = 0.2°$

Figure 27: The flux at the detector for two different orientations of E_{600}. In (a) the crystallite was oriented such that it fulfilled the Bragg condition, while it had been rotated 0.2° around the y-axis in (c). (b) and (d) show the flux along the two lines drawn in (a) and (c), respectively. The dashed lines in (a) and (c) correspond to the dashed curves in (b) and (d), respectively. The same applies to the dotted lines.

1 To repeat, E_i is short for an ellipsoidal sample with a base size of i unit cells. Similarly, H_i and C_i would correspond to a hexagonal prismatic sample and a cuboid sample, respectively.

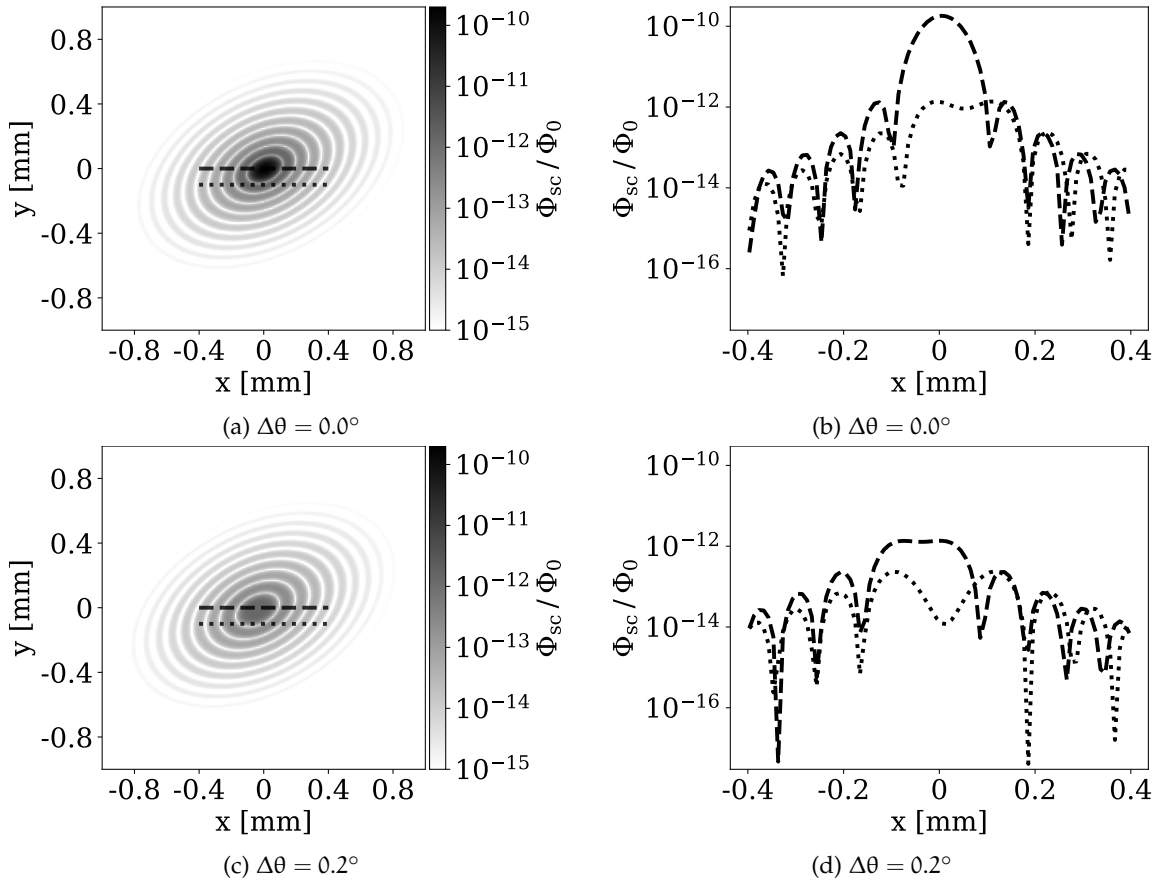

(a) $\Delta\theta = 0.0°$ (b) $\Delta\theta = 0.0°$

(c) $\Delta\theta = 0.2°$ (d) $\Delta\theta = 0.2°$

Figure 28: The flux at the detector for two different orientations of E_{150}. The condition are the same as in Figure 27. The flux for E_{150} was reduced less when rotating the crystallite compared to E_{600}, as expected from the discussion on the effects of crystallite size in Section 2.2.5.

5.2.3 *Intensity calculations - Rocking curve analysis*

Figure 29a demonstrates how the scattered intensity varied as a function of crystallite size when examining the (221) reflection of ellipsoidal crystallites. As expected, the amount of scattered intensity increased rapidly when increasing the crystallite size. The maximal value of I_{sc}/I_0 increased from 1.15×10^{-3} for E_{150} to 2.96×10^{-1} for E_{600}. All values are listed in Table 7. A value of approximately 30% could represent a significant reduction of the incoming beam due to wide-angle scattering. However, as stressed before, these values can only be considered as first estimates, as the normalisation method was most likely incorrect.

Nevertheless, it is interesting to see the range of rotation angles which yielded a significant signal compared to the maximum value for each crystallite size. This is presented in Figure 29b. The angular range yielding significant values was less than $\pm 0.1°$ for E_{600}, while it was approximately $\pm 0.4°$ for E_{150}. Both ranges are significantly narrower than what was assumed during the project work [49], as can be seen in Figure 16.

Table 7: The maximal value of I_{sc}/I_0 for three different crystallite sizes. The scattered intensities were calculated for the (221) reflection of E_{600}, E_{300} and E_{150}.

Base-size	I_{sc}/I_0
600	2.96×10^{-1}
300	1.85×10^{-2}
150	1.15×10^{-3}

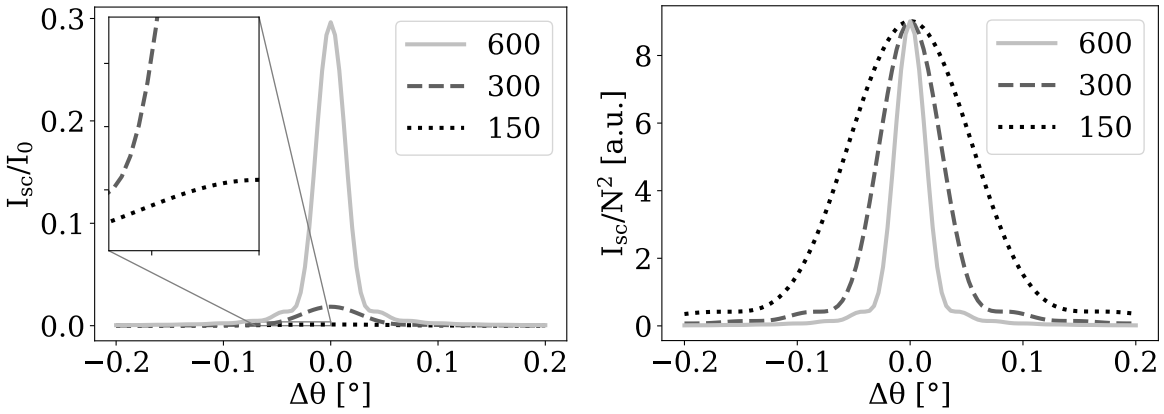

(a) (b)

Figure 29: Rocking curves from the (221) reflection of E_{600}, E_{300} and E_{150} showing the effects of crystallite size. As expected, the intensity increased with increasing crystallite size. In (b) the intensities have been normalised by a factor of N^2. It is evident that the peak intensity scales as N^2. Similarly, the width decreased with increasing crystallite size.

The effects of varying the crystallite shape have also been explored, and the results for H_{600}, E_{600} and C_{600} can be seen in Figure 30a. The rocking curves of E_{600} and C_{600} were almost identical, with only small variations, as seen in the inset of the figure. On the other hand, H_{600} displayed a sharper rocking curve with a taller peak. Initially, it might look like the total intensity scattered from H_{600} is significantly larger than the total intensity scattered from E_{600} and C_{600}. However, by integrating the scattered intensity over the rotation angles, one finds that the total intensity scattered from H_{600} only is 1% larger than the two others, i.e. comparable with the difference in the number of unit cells, as shown in Section 4.2.1. The total diffracted intensity, i.e. the intensity from all the orientations close to the Bragg condition, should increase as a linear function of N [56]. Since the three different shapes do not have exactly the same amount of unit cells, the observed discrepancy is likely caused by this.

From Figure 30a, it is evident that the scattered intensity at each orientation can depend on the crystallite shape. Therefore, depending on the rotation angle, H_{600} might scatter both more or less than E_{600} and C_{600}. However, the differences were small. Therefore, the shape of the crystallite is not expected to be a significant factor when considering the effects of Bragg scattering in a CDI experiment.

The rocking curve for three different reflections are presented in Figure 30b. All the rocking curves were calculated for a E_{600} crystallite. As expected from the difference in their unit cell structure factor, as listed in Table 3, more intensity is scattered of the (400) and (221) reflections compared to the (111) reflection. This indicates that significant reductions of the incoming beam are more likely to be a problem for the strongest reflections, as expected.

To summarise, crystallites with diameters in the range of 75 nm to 500 nm will only scatter a significant amount for a narrow angular range around the Bragg condition. For the smallest crystallites, this range was $\pm 0.4°$, while it was less than $\pm 0.1°$ for the largest crystallites. As mentioned in Section 5.1, by exchanging the intensity reduction filter used in [49] with this new range, the reconstruction quality improved significantly compared to what was seen in [49]. This improvement will be further studied in the following section.

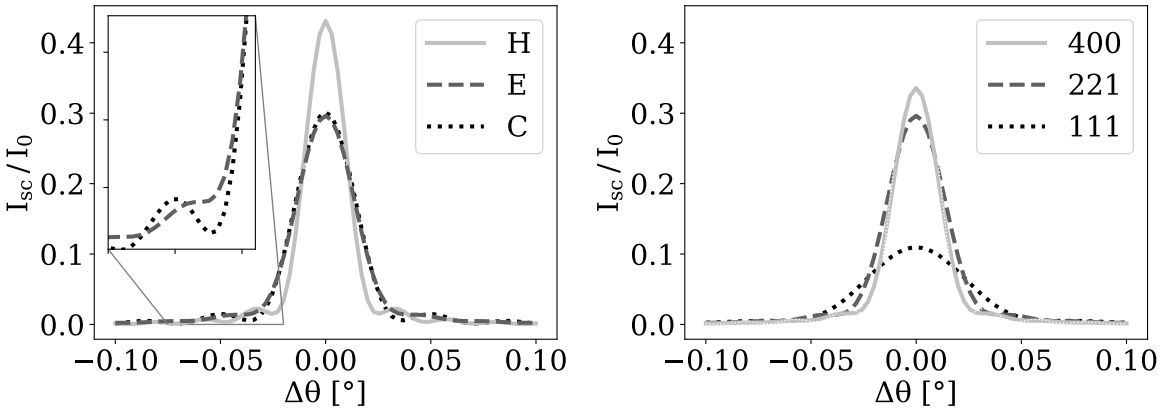

(a) Rocking curves from the (221)-reflection for the three examined shapes.

(b) Rocking curves from the three reflections (400), (221) and (111).

Figure 30: Rocking curves for crystallites having a base-size of 600. The effect of the crystallite shape is shown in (a). (b) displays the relation between the scattered intensity from the different reflections. As expected from Table 3, less intensity is scattered from the (111) reflection compared to the two other reflections. The scattered intensity approached zero at different angular deviations, but generally, they were all practically zero if the angular deviation was larger than 0.1°.

5.3 CDI SIMULATIONS

The density distributions of the reconstructed objects are presented in Figure 31. From the figure, it is evident that all the reconstructions have two well-defined peaks, indicating a successful reconstruction process. An increase in the width of the density distributions can be seen for the largest intensity reduction parameters, i.e. 30% to 60%. However, no obvious pattern could be seen for the lower intensity reduction parameters. For example, the reconstructions performed after applying a 20% intensity reduction generally seem to be better than the reconstructions where no intensity reduction had been applied. These variations are likely caused by the difference in the initial guess of the phase for each reconstruction. To better be able to compare the different intensity reduction parameters, the same 10 initial guesses of the phase should have been used for each parameter.

Two Gaussian functions were fitted to each of the histograms in Figure 31, as described in Section 4.3.4, and the parameters from this analysis are listed in Table 8. The standard deviations varied seemingly randomly between the lowest intensity reduction parameters. In fact, $\sigma_{l_0} = 1.02$ and $\sigma_{h_0} = 1.08$ were larger than all the other σ_{l_i} and σ_{h_i} for $i \leqslant 20$, except from $\sigma_{l_{15}}$, which was 1% larger than σ_{l_0}. In other words, no effect of Bragg scattering could be seen on the standard deviations of the density distributions as long as the intensity reductions were less than or equal to 20%. However, $\sigma_{l_{60}}$ and $\sigma_{h_{60}}$ were 66% and 53% larger than σ_{l_0} and σ_{h_0}, respectively, indicating a reduction in the reconstruction quality. These larger deviations were however not as prominent as those found in [49], indicating that the effects of Bragg scattering, if any, are weaker than first assumed in [49]. This is expected since the updated intensity reduction filter based on the results from the previous section is significantly narrower than the filter used in [49], resulting in less lost intensity.

The means of the distributions, μ_h and μ_l, were relatively stable. However, when increasing the intensity reduction, the peaks were separated slightly from each other. This separation can also be seen in Table 9, where the value of r_μ decreases from the correct value of 0.8 with increasing intensity reduction. No explanation for the separation has been found, but it indicates that the intensity reductions distort the phase retrieval process.

The values of a_l, a_h and r_a are also listed in Table 9. They will be discussed below.

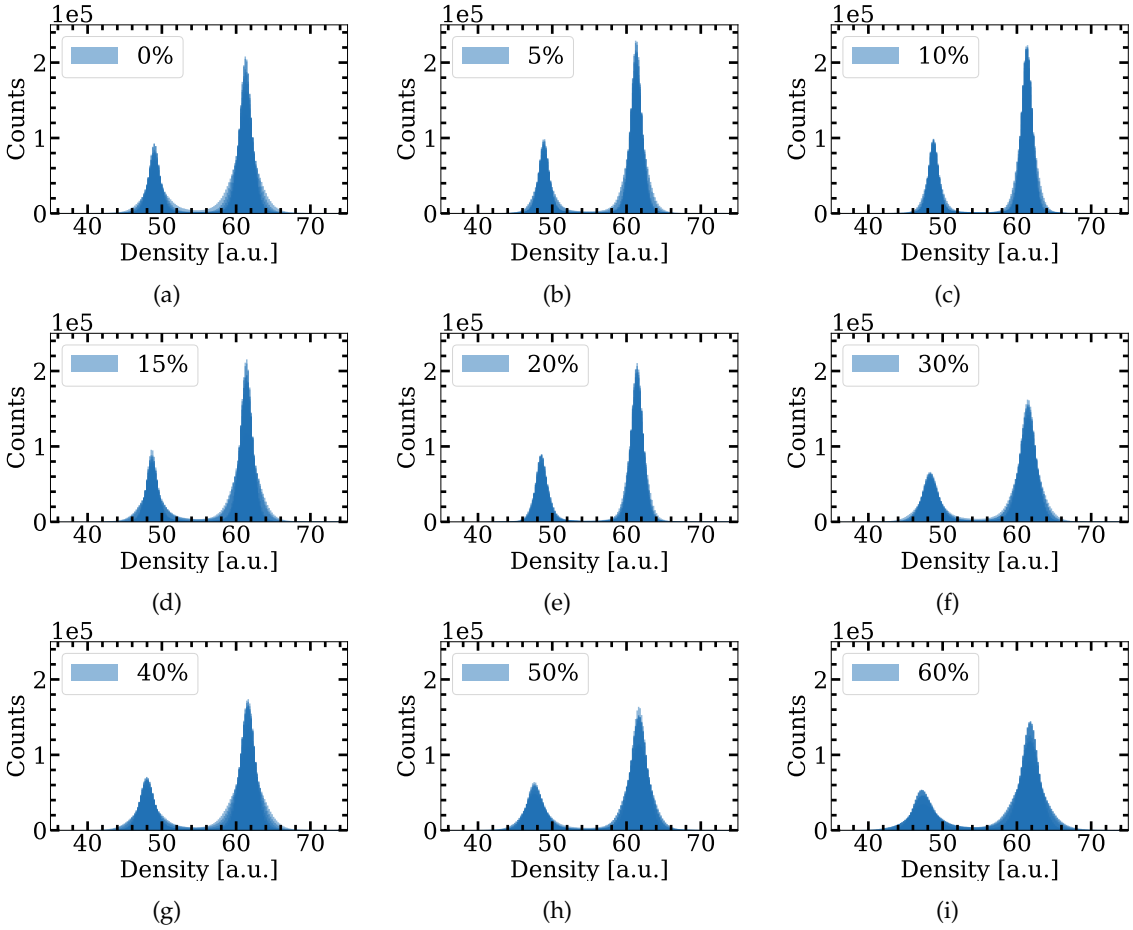

Figure 31: The density distributions for all the intensity reduction parameters. The intensity reduction is shown within the legend. For each parameter, the density distribution for the ten reconstructions is shown. The phase retrieval process was successful for all the intensity reduction parameters in the sense that all the reconstructions had two well-defined areas corresponding to the high- and low-density parts of the initial sample, as opposed to the findings in [49], which are shown in Figure 17. Each distribution has the same colour, given by the colour in the legend of each plot, meaning that the darker colours stem from overlapping distributions.

Table 8: Mean and standard deviation for the density distributions of the reconstructed object, shown in Figure 31, for all the intensity reduction parameters. All the values are given in arbitrary units.

Int. red.	μ_l	μ_h	σ_l	σ_h
0%	49.01 ± 0.06	61.28 ± 0.02	1.02 ± 0.33	1.08 ± 0.33
5%	48.89 ± 0.01	61.32 ± 0.01	0.85 ± 0.21	0.89 ± 0.21
10%	48.78 ± 0.01	61.35 ± 0.01	0.78 ± 0.14	0.83 ± 0.15
15%	48.69 ± 0.03	61.38 ± 0.01	1.03 ± 0.35	1.05 ± 0.33
20%	48.56 ± 0.03	61.41 ± 0.01	0.86 ± 0.11	0.89 ± 0.12
30%	48.37 ± 0.03	61.48 ± 0.01	1.24 ± 0.25	1.25 ± 0.24
40%	48.05 ± 0.05	61.57 ± 0.01	1.28 ± 0.37	1.25 ± 0.37
50%	47.72 ± 0.04	61.66 ± 0.01	1.35 ± 0.25	1.30 ± 0.25
60%	47.43 ± 0.09	61.74 ± 0.04	1.69 ± 0.39	1.56 ± 0.42

Table 9: The maximum values of the Gaussian functions, a_l and a_h, are given in arbitrary units. Their values have been divided by 10^4 compared to the raw data in Figure 31. The values for r_μ and r_a were calculated from the a_l and a_h value for each reconstruction, i.e. not calculated from the a_l and a_h values in this table, explaining the differences in their uncertainties.

Int. red.	a_l	a_h	r_μ	r_a
0%	8.68 ± 2.09	19.70 ± 4.66	0.80 ± 0.00	2.42 ± 0.03
5%	10.02 ± 1.88	23.11 ± 4.39	0.80 ± 0.00	2.44 ± 0.04
10%	10.65 ± 1.52	24.28 ± 3.63	0.80 ± 0.00	2.43 ± 0.04
15%	8.69 ± 2.33	20.30 ± 5.14	0.79 ± 0.00	2.42 ± 0.03
20%	9.58 ± 1.12	22.48 ± 2.62	0.79 ± 0.00	2.43 ± 0.03
30%	6.81 ± 1.13	16.39 ± 2.77	0.79 ± 0.00	2.42 ± 0.02
40%	6.89 ± 1.60	17.05 ± 4.00	0.78 ± 0.00	2.41 ± 0.03
50%	6.26 ± 1.02	15.80 ± 2.92	0.77 ± 0.00	2.42 ± 0.02
60%	5.14 ± 1.11	13.57 ± 3.32	0.77 ± 0.00	2.40 ± 0.02

As evident from Table 9, the values of a_l and a_h were lower for the highest intensity reduction parameters. Again, a larger value for the a-values corresponds to a higher degree of certainty, as the histograms were collected from approximately the same number of voxels. $a_{l_{60}}$ and $a_{h_{60}}$ decreased with 41% and 31% compared to a_{l_0} and a_{h_0}, respectively, indicating a reduction in the reconstruction quality.

The values of r_a, i.e. the ratio between the areas under the two Gaussian functions, remained rather stable. However, they were all above the initial value of 2.34. From Figure 33 it can be seen that the density distributions are not exact Gaussians. It is therefore expected that the area under the curves might deviate slightly from the actual value.

As explained in Section 4.3.4, the average of the 10 reconstruction for each intensity reduction parameter has also been calculated. The density distributions of these average objects are presented in Figure 32. The distributions were significantly narrower than the ones shown in Figure 31, i.e. the distributions from the individual reconstructions. This highlights how the density variations of the reconstructed objects are mostly random fluctuations around the correct values. By finding the average of 10 reconstructions, these fluctuations were seen to diminish significantly. This averaging process is commonly applied in CDI experiments, exactly to limit the effects of random fluctuations.

Even though the results improved further when averaging the reconstructed objects, a reduction in the reconstruction quality can still be seen for the highest intensity reduction parameters. This reduction is also evident in Table 10, where $\sigma_{l_0} = 0.47$ and $\sigma_{h_0} = 0.50$ while $\sigma_{l_{60}} = 1.30$ and $\sigma_{h_{60}} = 0.99$, i.e. an increase of 112% and 98%, respectively. However, no clear trend could be seen for the lower intensity reductions, except for the increase in the difference between μ_h and μ_l when increasing the intensity reduction.

The deviations from the initial structure have also been studied. The results can be seen in Figure 33 and Table 11. The deviations are relatively small, mostly less than 0.025, corresponding to a relative deviation of 3.1% and 2.5% for the low- and high-density region, respectively. However, the deviations are seen to increase for the largest intensity reduction parameters. Additionally, the histograms for the three largest reductions deviate from the expected Gaussian shape. No explanation has been found for this, but it indicates that the intensity reductions can lead to systematic errors in the reconstruction process.

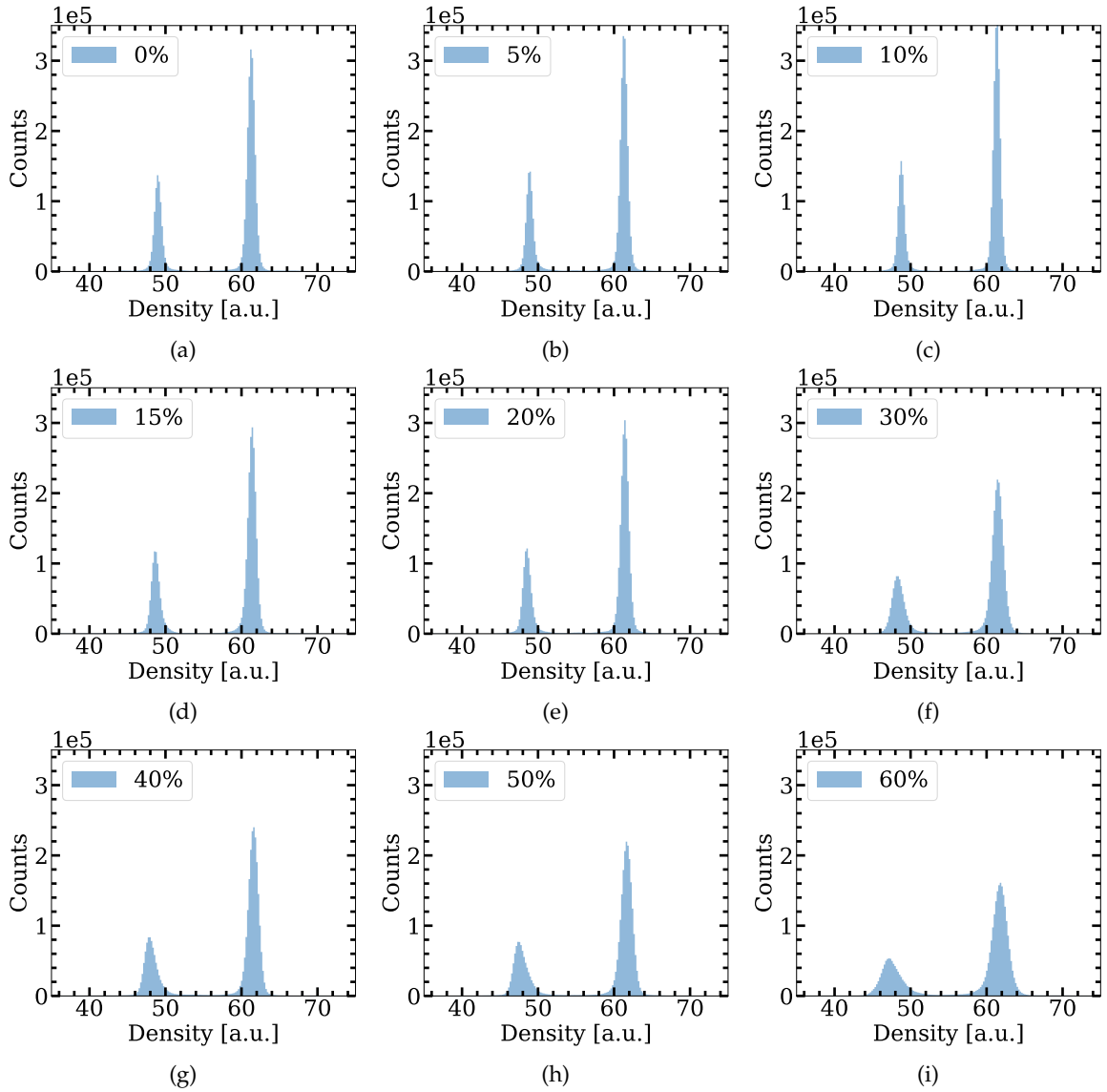

Figure 32: The density distributions of the average objects for all the intensity reduction parameters. Note that the y-axis has been extended compared to Figure 17 and 31 to account for the tall peaks. However, the scale has been kept the same for ease of comparison.

Table 10: Mean and standard deviation of the mean density distributions for different intensity reduction parameters. The mean density values, and hence the standard deviations, of the Gaussian functions are given in arbitrary units.

Int. red.	μ_l	μ_h	σ_l	σ_h
0%	49.01	61.28	0.47	0.50
5%	48.89	61.32	0.45	0.46
10%	48.78	61.35	0.41	0.44
15%	48.68	61.38	0.55	0.54
20%	48.54	61.42	0.54	0.52
30%	48.34	61.49	0.80	0.73
40%	48.00	61.58	0.79	0.66
50%	47.64	61.67	0.88	0.73
60%	47.37	61.77	1.30	0.99

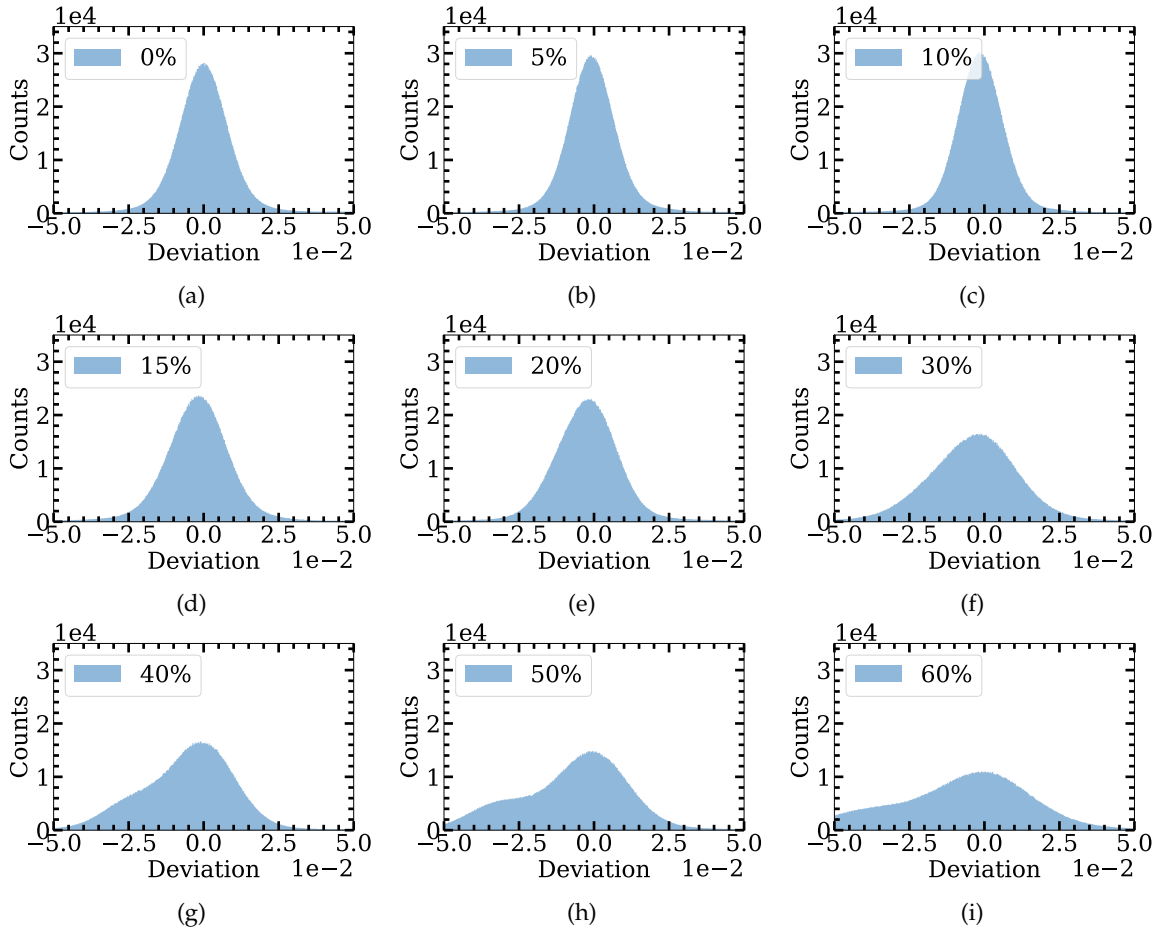

Figure 33: The deviation between the average objects and the initial object for all the intensity reduction parameters. The normalisation was done by dividing each average reconstruction with their respective μ_h value, which can be found in Table 10. Since μ_h shifted towards larger values when increasing the intensity reduction, it is natural that the deviations will be shifted towards negative values with an increasing intensity reduction parameter.

Table 11: Mean and standard deviation of the Gaussian functions that were fitted to the deviation data shown in Figure 33. Compared with the raw data shown in Figure 33, the values have been multiplied by a factor of 1000 for ease of readability. Note from Figure 33 that the deviation distributions for the three largest intensity reductions deviated from the assumed Gaussian shape. These values have therefore been marked with a $*$.

Int. red.	μ	σ
0%	-0.06 ± 0.02	8.00 ± 0.02
5%	-0.81 ± 0.02	7.58 ± 0.02
10%	-1.43 ± 0.02	7.48 ± 0.02
15%	-1.83 ± 0.02	9.62 ± 0.02
20%	-2.39 ± 0.02	9.87 ± 0.02
30%	-3.23 ± 0.04	14.09 ± 0.04
40%*	-3.65 ± 0.12	14.53 ± 0.12
50%*	-4.26 ± 0.21	16.98 ± 0.21
60%*	-4.82 ± 0.19	21.57 ± 0.20

5.4 FUTURE WORK

The sections above have given indications that Bragg scattering might have a negative impact on the phase retrieval process in a CDI experiment. Even when assuming that the Bragg scattering will only affect the CDI diffraction pattern for a narrow range of sample orientations, i.e. $\pm 0.1^{\circ}$, a reduction in the reconstruction quality could be seen. However, there are several parts that should be further analysed. A simple first step would be to exchange the phase retrieval algorithm used in this thesis to see if other algorithms are more resilient against the intensity losses. Nevertheless, before continuing with further experimentations on the phase retrieval algorithm, there is especially one part that should be improved. That is the part on the normalisation of the scattered intensity. Without a measure on the amount of scattered intensity, changing the phase retrieval algorithm would not be worth much, as the calculations have shown that Bragg scattering will not affect the reconstruction quality for the weakest intensity reduction. Of course, this could change, i.e. Bragg scattering could affect the results even for weak reductions, if one were to take more factors present in real experiments, such as a beamstop, noise and missing wedges into account. These have been omitted in the calculations performed in this thesis, but must be considered before drawing any conclusions. Therefore, before concluding on whether Bragg scattering might have an impact on real experiments, the simulations must mimic the true conditions to a larger degree, both with regards to the amount of scattered intensity and by including a beamstop and noise etc.

In addition to numerical calculations on the amount of scattered intensity when the crystallite fulfils the Bragg condition, quantitative experiments that measure the relation between the incoming and scattered intensity should be performed. It would be difficult to reproduce the results seen in the scattering calculations performed in this thesis, both due to the small detector pixels and rotation angles, but the overall trends should be similar.

6 CONCLUSION

This thesis has further proven that Bragg scattering might have a negative impact on the phase retrieval process in a CDI experiment, as previously suggested in [49]. However, the negative effects were only seen when assuming that more than 20% of the incoming beam was scattered to the wide-angle detector. Therefore, the amount of scattered intensity compared to the incoming intensity must be decided before one can draw any conclusions. This could likely be found through a more thorough numerical analysis, or by designing a suitable experiment.

Either way, if the intensity reductions were to be as large as proposed in this thesis and in [49], the negative effects would still not be as severe as previously thought. Simulated rocking curves of finite aragonite crystallites have proven that a wide-angle signal is only obtained for a narrow range of rotations of the sample. The examined crystallites had diameters ranging from 75 nm to 500 nm. For the smallest crystallites, a signal could be detected up until the point where the crystallites were rotated approximately 0.4° away from the Bragg condition around the y-axis, i.e. the axis parallel to the scattering planes and normal to the incoming beam. This range was even narrower for the largest crystallites, where the scattered signal was essentially zero if the crystallites were rotated more than 0.1° away from the Bragg condition.

Both of these ranges were significantly narrower than what had been assumed in [49]. The CDI simulations were therefore repeated, this time with the updated information about the angular range. This time, the applied phase retrieval algorithm was able to reconstruct the initial object for all the intensity reduction parameters, and only a minor increase in the local deviations of the density was seen when comparing the largest intensity reduction parameters with the reconstructions where no intensity reduction had been applied.

All in all, the author finds it unlikely that Bragg scattering will have a significant negative impact on the phase retrieval process in CDI experiments, based on the findings in this thesis. Throughout this thesis, only small variations have been found, and they were only found by assuming that approximately 50% of the incoming beam is scattered to the wide-angle detector.

However, there are many parameters that have not been examined. Therefore, several other effects, such as a beamstop, missing wedges and noise should also be explored before drawing any final conclusions.

BIBLIOGRAPHY

[1] Sytle M. A. and Ishmael H. "The orthorombic structure of $CaCO_3$, $SrCO_3$, $PbCO_3$ AND $BaCO_3$: Linear structural trends." In: *Can. Mineral.* 47.5 (Oct. 2009), pp. 1245–1255.

[2] J. Als-Nielsen and D. McMorrow. *Elements of Modern X-ray Physics*. 2nd. Chichester, West Sussex, UK: John Wiley & Sons, Ltd, 2011.

[3] R. Ballabriga, M. Campbell, E. Heijne, X. Llopart, L. Tlustos, and W. Wong. "Medipix3: A 64k pixel detector readout chip working in single photon counting mode with improved spectrometric performance." In: *Nucl. Instrum. Methods Phys. Res. A: Accel. Spectrom. Detect. Assoc. Equip.* 633 (2011), S15–S18.

[4] R. H. T. Bates. "Fourier phase problems are uniquely soluble in more than one dimension. I: underlying theory." In: *Optik* 61.3 (Nov. 1982), pp. 247–262.

[5] R. H. T. Bates. "Uniqueness of solutions to two-dimensional fourier phase problems for localized and positive images." In: *Comput. Gr. Image Process.* 25.2 (1984), pp. 205–217.

[6] R. H. T. Bates and W. R. Fright. "Composite two-dimensional phase-restoration procedure." In: *J. Opt. Soc. Am.* 73.3 (1983), pp. 358–365.

[7] R. H. T. Bates and W. R. Fright. "Two-Dimensional Phase Restoration." In: *Fourier Techniques and Applications*. Ed. by John F. Price. Boston, MA: Springer US, 1985, pp. 121–148.

[8] B. W. Batterman and H. Cole. "Dynamical Diffraction of X Rays by Perfect Crystals." In: *Rev. Mod. Phys.* 36.3 (July 1964), pp. 681–717.

[9] W. L. Bragg. "The structure of aragonite." In: *Proc. R. Soc. A* 105.729 (1924), pp. 16–39.

[10] Y. M. Bruck and L. G. Sodin. "On the ambiguity of the image reconstruction problem." In: *Opt. Commun.* 30.3 (1979), pp. 304–308.

[11] H. N. Chapman and K. A. Nugent. "Coherent lensless X-ray imaging." In: *Nat. Photon* 4.12 (2010), pp. 833–839.

[12] B. Chattopadhyay, A. S. Madathiparambil, F. K. Mürer, P. Cerasi, Y. Chushkin, F. Zontone, A. Gibaud, and D. W. Breiby. "Nanoscale imaging of shale fragments with coherent X-ray diffraction." In: *J. Appl. Crystallogr.* 53.6 (Dec. 2020), 1562–1569.

[13] D. T. Cromer. "Anomalous dispersion corrections computed from self-consistent field relativistic Dirac–Slater wave functions." In: *Acta Crystallogr.* 18.1 (1965), pp. 17–23.

[14] D. T. Cromer and J. T. Waber. "Scattering factors computed from relativistic Dirac–Slater wave functions." In: *Acta Crystallogr.* 18.1 (1965), pp. 104–109.

[15] T. Ekeberg et al. "Three-Dimensional Reconstruction of the Giant Mimivirus Particle with an X-Ray Free-Electron Laser." In: *Phys. Rev. Lett.* 114.9 (Mar. 2015), pp. 098–102.

[16] V. Favre-Nicolin, J. Coraux, M. Richard, and H. Renevier. "Fast computation of scattering maps of nanostructures using graphical processing units." In: *J. Appl. Crystallogr.* 44.3 (Apr. 2011), pp. 635–640.

[17] V. Favre-Nicolin, G. Girard, S. Leake, J. Carnis, Y. Chushkin, J. Kieffer, P. Paleo, M. Richard, et al. "PyNX: high-performance computing toolkit for coherent X-ray imaging based on operators." In: *J. Appl. Crystallogr.* 53.5 (Aug. 2020), 1404–1413.

[18] J. R. Fienup. "Reconstruction of an object from the modulus of its Fourier transform." In: *Opt. Lett.* 3.1 (1978), pp. 27–29.

[19] J. R. Fienup. "Phase retrieval algorithms: a comparison." In: *Appl. Opt.* 21 (Aug. 1982), pp. 2758–2769.

[20] J. R. Fienup. "Reconstruction of a complex-valued object from the modulus of its Fourier transform using a support constraint." In: *J. Opt. Soc. Am. A* 4.1 (1987), pp. 118–123.

[21] J. R. Fienup and C. C. Wackerman. "Phase-retrieval stagnation problems and solutions." In: *J. Opt. Soc. Am. A* 3.11 (1986), pp. 1897–1907.

[22] A. G. Fox, M. A. O'Keefe, and M. A. Tabbernor. "Relativistic Hartree–Fock X-ray and electron atomic scattering factors at high angles." In: *Acta Crystallogr. A* 45.11 (1989), pp. 786–793.

[23] Dennis F. Gardner et al. "Subwavelength coherent imaging of periodic samples using a 13.5 nm tabletop high-harmonic light source." In: *Nat. Photonics* 11.4 (2017), pp. 259–263.

[24] R. W. Gerchberg and W. O. Saxton. "A practical algorithm for the determination of phase from image and diffraction plane pictures." In: *Optik* 35.2 (1972), pp. 237–246.

[25] R. W. Gerchberg and W. O. Saxton. "Comment on 'A method for the solution of the phase problem in electron microscopy'." In: *J. Phys. D: Appl. Phys.* 6.5 (1973), p. L31.

[26] D. J. Griffiths and D. F. Schroeter. *Introduction to Quantum Mechanics*. 3rd ed. Cambridge University Press, 2018.

[27] M. Guizar-Sicairos and J. R. Fienup. "Understanding the twin-image problem in phase retrieval." In: *J. Opt. Soc. Am. A* 29.11 (2012), pp. 2367–2375.

[28] M. Hayes. "The reconstruction of a multidimensional sequence from the phase or magnitude of its Fourier transform." In: *IEEE Trans. Acoust* 30.2 (1982), pp. 140–154.

[29] M. Holler, M. Guizar-Sicairos, E. H. R. Tsai, et al. "High-resolution non-destructive three-dimensional imaging of integrated circuits." In: *Nature* 543 (2017), pp. 402–406.

[30] I. Juvells, S. Vallmitjana, A. Carnicer, and J. Campos. "The role of amplitude and phase of the Fourier transform in the digital image processing." In: *Am. J. Phys.* 59.8 (1991), pp. 744–748.

[31] T. Latychevskaia. "Iterative phase retrieval in coherent diffractive imaging: practical numbers." In: *Appl. Opt.* 57.25 (2018), pp. 7187–7197.

[32] D. Liberman, J. T. Waber, and Don T. Cromer. "Self-Consistent-Field Dirac-Slater Wave Functions for Atoms and Ions. I. Comparison with Previous Calculations." In: *Phys. Rev.* 137.1A (1965), A27–A34.

[33] S. Marchesini, H. He, H. N. Chapman, S. P. Hau-Riege, A. Noy, M. R. Howells, U. Weierstall, and J. C. H. Spence. "X-ray image reconstruction from a diffraction pattern alone." In: *Phys. Rev. B* 68.14 (2003), p. 140101.

[34] J. Miao, P. Charalambous, J. Kirz, and D. Sayre. "Extending the methodology of X-ray crystallography to allow imaging of micrometre-sized non-crystalline specimens." In: *Nature* 400.6742 (1999), pp. 342–344.

[35] J. Miao, T. Ishikawa, I. K. Robinson, and M. M. Murnane. "Beyond crystallography: Diffractive imaging using coherent x-ray light sources." In: *Science* 348.6234 (2015), pp. 530–535.

[36] J. Miao, R. L. Sandberg, and C. Song. "Coherent X-Ray Diffraction Imaging." In: *IEEE J. Sel. Top. Quantum Electron.* 18.6742 (2012), pp. 399–410.

[37] J. Miao, D. Sayre, and H. N. Chapman. "Phase retrieval from the magnitude of the Fourier transforms of nonperiodic objects." In: *J. Opt. Soc. Am. A* 15.6 (1998), pp. 1662–1669.

[38] T. Narayanan, M. Sztucki, P. Van Vaerenbergh, J. Léonardon, J. Gorini, L. Claustre, F. Sever, J. Morse, and P. Boesecke. "A multipurpose instrument for time-resolved ultra-small-angle and coherent X-ray scattering." In: *J. Appl. Crystallogr.* 51.6 (2018), pp. 1511–1524.

[39] H. Nyquist. "Certain Topics in Telegraph Transmission Theory." In: *Trans. AIEE* 47.2 (1928), pp. 617–644.

[40] A.V. Oppenheim and J.S. Lim. "The importance of phase in signals." In: *Proc. IEEE* 69.6 (1981), pp. 529–541.

[41] F. Pfeiffer. "X-ray ptychography." In: *Nat. Photon* 12.1 (Jan. 2018), pp. 9–17.

[42] P. Raimondi et al. "The Extremely Brilliant Source storage ring of the European Synchrotron Radiation Facility." In: *Commun. Phys.* 6.1 (2023).

[43] I. K. Robinson, I. A. Vartanyants, G. J. Williams, M. A. Pfeifer, and J. A. Pitney. "Reconstruction of the Shapes of Gold Nanocrystals Using Coherent X-Ray Diffraction." In: *Phys. Rev. Lett.* 87.19 (2001), p. 195505.

[44] J. M. Rodenburg, A. C. Hurst, A. G. Cullis, B. R. Dobson, F. Pfeiffer, O. Bunk, C. David, K. Jefimovs, and I. Johnson. "Hard-X-Ray Lensless Imaging of Extended Objects." In: *Phys. Rev. Lett.* 98.3 (2007), p. 034801.

[45] T. Salditt and M. Osterhoff. "X-ray Focusing and Optics." In: *Nanoscale Photonic Imaging*. June 2020, pp. 71–124.

[46] S. Sasaki. *Numerical tables of anomalous scattering factors calculated by the Cromer and Liberman's method*. Feb. 1989.

[47] D. Sayre. "Some implications of a theorem due to Shannon." In: *Acta Cryst.* 5 (1952), p. 843.

[48] C.E. Shannon. "Communication in the Presence of Noise." In: *Proc. IRE* 37.1 (1949), pp. 10–21.

[49] S. Stene. *Numerical Simulations of Crystalline Samples in Coherent X-Ray Diffraction Imaging - Investigating the effects of Bragg scattering*. Dec. 2022.

[50] A. Szabo and N. S. Ostlund. *Modern Quantum Chemistry: Introduction to Advanced Electronic Structure Theory*. Dover Books on Chemistry. Dover Publications, 1996.

[51] Y. Takahashi, Y. Nishino, R. Tsutsumi, N. Zettsu, E. Matsubara, K. Yamauchi, and T. Ishikawa. "High-resolution projection image reconstruction of thick objects by hard x-ray diffraction microscopy." In: *Phys. Rev. B* 82.21 (2010), p. 214102.

[52] P. Thériault-Lauzier, M. Spaziano, B. Vaquerizo, J. Buithieu, G. Martucci, and N. Piazza. "Computed Tomography for Structural Heart Disease and Interventions." In: *Interv Cardiol* 10.3 (2015), 149—154.

[53] F. van der Veen and F. Pfeiffer. "Coherent x-ray scattering." In: *J. Phys. Condens. Matter.* 16.28 (2004), p. 5003.

[54] A. Vretblad. *Fourier Analysis and Its Applications*. 1st. New York, NY: Springer, 2010.

[55] H. K. Wagenfeld. "The angular dependence of X-ray dispersion corrections." In: *Z. Phys. B* 65.4 (1987), pp. 437–441.

[56] B. E. Warren. *X-ray Diffraction*. Dover Publications, 1990.

[57] E. T. Whittaker. "On the Functions which are represented by the Expansions of the Interpolation-Theory." In: *Proc. R. Soc. Edinb* 35 (1915), 181–194.

[58] G. J. Williams, M. A. Pfeifer, I. A. Vartanyants, and I. K. Robinson. "Three-Dimensional Imaging of Microstructure in Au Nanocrystals." In: *Phys. Rev. Lett.* 90.17 (2003), p. 175501.

[59] P. Willmott. *Introduction to Synchrotron Radiation*. 1st. Chichester, West Sussex, UK: John Wiley & Sons, Ltd, 2011.

[60] J. Wu and J. Spence. "Reconstruction of complex single-particle images using charge-flipping algorithm." In: *Acta cryst.* 61 (Apr. 2005), pp. 194–200.

[61] G. Xiong, O. Moutanabbir, M. Reiche, R. Harder, and I. Robinson. "Coherent X-Ray Diffraction Imaging and Characterization of Strain in Silicon-on-Insulator Nanostructures." In: *Adv. Mater.* 26.46 (2014), pp. 7747–7763.

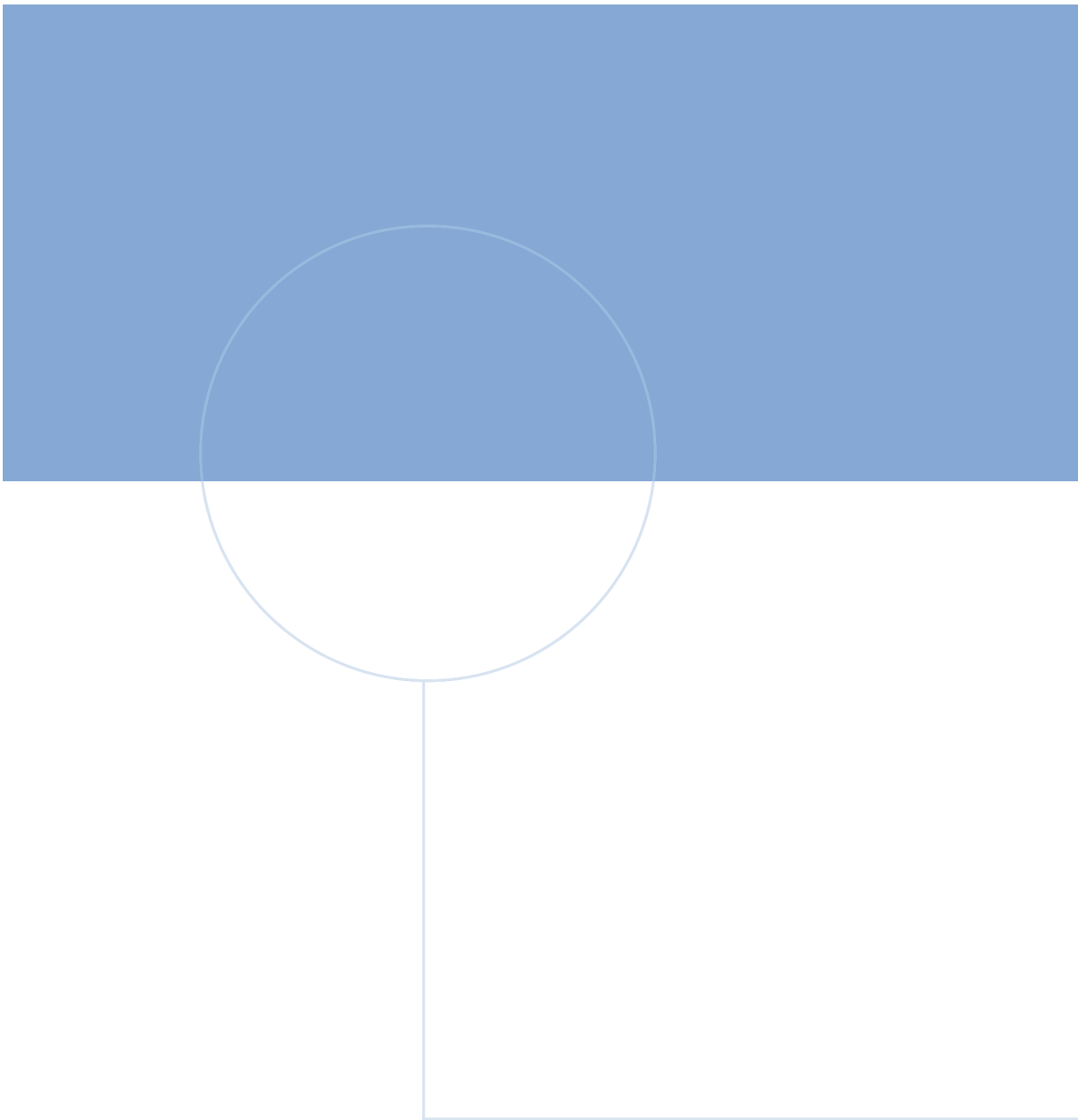

NTNU

Norwegian University of
Science and Technology